Oceanic Frontal Turbulence

PETER P. SULLIVAN[a] AND JAMES C. MCWILLIAMS[b]

[a] *National Center for Atmospheric Research, Boulder, Colorado*
[b] *Department of Atmospheric and Oceanic Sciences, University of California, Los Angeles, Los Angeles, California*

(Manuscript received 27 February 2023, in final form 10 November 2023, accepted 20 November 2023)

ABSTRACT: Upper-ocean turbulence results from a complex set of interactions between submesoscale turbulence and local boundary layer processes. The interaction between larger-scale currents and turbulent fluctuations is two-way: large-scale shearing motions generate turbulence, and the resulting coherent turbulent fluxes of momentum and buoyancy feed back onto the larger flow. Here we examine the evolution and role of turbulence in the intensification, instability, arrest, and decay (i.e., the life cycle) of a dense filament undergoing frontogenesis in the upper-ocean boundary layer, i.e., cold filament frontogenesis (CFF). This phenomenon is examined in large-eddy simulations (LES) with resolved turbulent motions in large horizontal domains using 10^9 grid points. The boundary layer turbulence is generated by surface buoyancy loss (cooling flux) and is allowed to freely interact with an initially imposed cold filament, and the evolution is followed through the frontal life cycle. Two control parameters are explored: the initial frontal strength $M^2 = \partial_x b$ and the surface flux Q_*. The former is more consequent: initially weaker fronts sharpen more slowly and become arrested at a later time with a larger width. This reflects a competition between the frontogenetic rate induced by the secondary circulation associated with vertical momentum mixing by the turbulence and the instability rate for the along-filament shear flow. The frontal turbulence is energized by the shear production of the latter, is nonlocally transported away from the primary production zone at the filament centerline, and cascades to dissipation in a broad region surrounding the filament. The turbulent momentum fluxes arresting the frontogenesis are supported across a wide range of horizontal scales.

KEYWORDS: Boundary layer; Density currents; Frontogenesis/frontolysis

1. Introduction

In the upper ocean, on spatial scales lying between mesoscale eddies and boundary layer turbulence, are submesoscale currents (SMCs). They extract kinetic and potential energy from the former and deliver at least some of it to the latter en route to dissipation (McWilliams 2016; Gula et al. 2021; Taylor and Thompson 2023). A dominant SMC process is the frontogenesis of horizontal buoyancy gradients at the surface due to either mesoscale strain flows or turbulent vertical momentum flux [a.k.a. turbulent thermal wind (TTW)] (Hoskins and Bretherton 1972; McWilliams 2021). We use "front" generally to include both one-sided and two-sided density gradients; the two-sided filaments considered here are primarily cold or dense in their center compared to their edges (McWilliams et al. 2009) A compelling question is the outcome of frontogenesis, i.e., what is a typical frontal life cycle?

The question is methodologically difficult to answer because it involves a large active range of scales (roughly 10–10^4 m) during a short period of time (from hours to days), and its associated patterns are quite complex. The nature of frontogenesis is to collapse the cross-frontal width at a superexponential rate, causing the velocity shear to increase in pace. This, in turn, amplifies the unstable growth rate for the frontal shear, injecting energy into turbulence, inducing momentum and buoyancy mixing, and halting the frontogenesis (i.e., causing frontal arrest). Ultimately, in the absence of new mesoscale energy injection, the arrested SMC front and its energy cascade must decay back to whatever background level of boundary layer turbulence is sustained by the surface stress and buoyancy flux. While this general conception of a frontal life cycle seems plausible, it as yet has rather few realizations in measurements and models (D'Asaro et al. 2011, 2018; Sullivan and McWilliams 2018, hereafter SM18; Sullivan and McWilliams 2019, hereafter SM19); so much remains to be further explored.

The phenomena of frontogenesis and frontal instability do not necessarily involve turbulence (though TTW frontogenesis is based on it), but its presence will influence these processes (Spall 1997; Thomas and Lee 2005; Brucker and Sarkar 2007; McWilliams et al. 2015; Kaminski and Smyth 2019; Bodner et al. 2020, 2023), and its emergence is inescapable in a full frontal life cycle.

This paper has the dual purposes of making the life cycle stages more explicit and further examining the turbulence in the later stages of the cycle. While background mesoscale flows, surface wind stress, and surface gravity waves all can be influential on the frontal evolution (McWilliams 2017, 2018; SM18; SM19; Yuan and Liang 2021), here the problem is posed in what seems a maximally simple configuration: the evolution of an initially two-dimensional, dense, surface-layer filament under convective buoyancy-layer forcing above a stably stratified interior. We explore two primary control parameters. One is the initial filament strength,

$$\frac{M^2}{f^2} = \frac{1}{f^2}\max[\partial_x\langle b\rangle]\ (z = 0,\ t = 0)\,, \tag{1}$$

Corresponding author: Peter P. Sullivan, pps@ucar.edu

DOI: 10.1175/JPO-D-23-0033.1

TABLE 1. Simulation cases.

Simulation	M^2/f^2	Cooling Q_* (W m^{-2})	w_* (m s^{-1})	ζ_{peak}	TKE_{peak}	t_p (h)	ℓ_w (m)	ζ_o (s^{-1})
S100	128.6	100	0.0137	12.9	25.5	6.13	100	8.70
S15	128.6	15	0.007 28	12.8	35.1	6.67	158	9.97
M100	83.59	100	0.0137	10.2	14.1	9.75	185	5.52
W100	46.4	100	0.0137	2.47	4.43	33.1	211	3.76
W15	46.4	15	0.007 28	2.58	4.70	28.1	211	4.10
VW100	10.0	100	0.0137	~1.4	~1.8	~103.8	396	1.68

where $b = -g\rho/\rho_o$ is the buoyancy, ρ and ρ_o are the density and reference density, respectively, f is the Coriolis frequency, x and z are the across-filament and vertical coordinates, respectively, and the angle brackets are an alongfront (y) average. The other control parameter is the surface heat flux Q_* in a simple fluid with $\rho \propto -\theta$, the temperature.

To address the role of frontal turbulence in a frontal life cycle in a model, a large-eddy simulation (LES) spanning both the frontal and turbulence currents is necessary. Here the flow is initialized by an artificial relaxation damping toward a specified $\langle b \rangle(x, z)$ in the presence of surface buoyancy flux and an initial mixed layer and pycnocline stratification profile. Once the flow is fully turbulent and the filament velocity $\langle \mathbf{u} \rangle(x, z)$ has adjusted to $\langle b \rangle$, the relaxation term is removed and the flow freely evolves in the usual manner of large-eddy simulation; see SM18 for details.

Frontal dynamics has a large literature rooted in the atmosphere (e.g., Hoskins and Bretherton 1972; Hoskins 2003), while its investigations for the ocean are more recent. Many circulation models that resolve submesoscale currents exhibit surface fronts and frontogenesis (McWilliams 2016), but their grids are too coarse to adequately resolve the turbulent fluid dynamics of the instability and arrest processes, except implicitly through their subgrid-scale (SGS) parameterizations. The literature on oceanic frontal LES studies is now a substantial one. A partial list includes Hamlington et al. (2014), Pham and Sarkar (2018, 2019), Skyllingstad and Samelson (2012), Skyllingstad et al. (2017), Skyllingstad and Samelson (2020), Verma et al. (2019, 2022), and Pham et al. (2023), and we hesitate to make a detailed summary of each of them here. For most of these the focus is on the spindown of a front through its instabilities, with less attention to the frontogenesis and arrest processes. For many of these idealized simulations, coexisting boundary layer turbulence is absent, although, of course, not very often in nature. It is known that classical instabilities (e.g., distinct Kelvin–Helmholtz overturns) can be inhibited by turbulence (Kaminski and Smyth 2019). And, also of course, no idealized simulation can encompass the full range of processes causing forward energy cascades toward dissipation that occur in the ocean.

For many of these, the primary frontal instability type is baroclinic instability (also called mixed layer instability), but instances of horizontal and vertical (a.k.a. Kelvin–Helmholtz) shear instabilities and symmetric instability are also found; all these instabilities do lead to enhanced frontal turbulence, of course, as also seen in measurements (Johnston et al. 2011; D'Asaro et al. 2011).

Frontogenesis in combination with local turbulent processes, including wind, convection, and Langmuir turbulence, also impacts the mixing of neutral and buoyant tracers, microplastics, and pollutants. Submesoscale and local turbulence can act to induce surface convergence and subduction of scalars in both modeling and observational studies (e.g., Kukulka and Brunner 2015; Taylor 2018; Cohen et al. 2019; Wenegrat et al. 2020; Qu et al. 2022; Dingwall et al. 2023; Taylor and Thompson 2023). Recently, Wenegrat et al. (2020) observed enhanced scalar mixing across the Gulf Stream front under a complex set of forcing conditions with winds, waves, and convection. They attribute the mixing to so-called "shear dispersion," a vertical mixing process that combines differential advection in a horizontal plane with enhanced transverse vertical diffusion (Taylor 1953; Csanady 1973; Young et al. 1982). Taylor (2018) applies constant slantwise large-scale periodic forcing, primarily 2.5D "LES," to examine a convectively driven mixed layer. The large-scale forcing is held constant allowing an assumption of horizontal periodicity in x and y. Crowe and Taylor (2019) adopts a similar assumption about the large-scale forcing but uses direct numerical simulation to examine ocean boundary layer (OBL) mixing at Rossby numbers $\sim O(1)$ at finite Ekman numbers. Skyllingstad and Samelson (2020) considers the transition from symmetric to baroclinic instability for finite width fronts with a constant vertical temperature structure with no preexisting turbulence. The simulation of Wenegrat et al. (2020) applies time-dependent forcing but also adopts the horizontally periodic forcing assumption as in Taylor (2018). As configured the simulations of Taylor (2018) and Crowe and Taylor (2019) effectively impose an infinite width front (Skyllingstad and Samelson 2020), and thus do not answer the role of horizontal shear and preexisting turbulence forcing a submesoscale filament undergoing frontogenesis.

As stated above, our intent in this paper is to encompass the full life cycle of a front and its turbulence in a highly idealized configuration. Because the processes causing frontogenesis have already received much attention, in this paper we address three other life cycle questions:

1) What is the space–time structure of the frontal turbulence?
2) How does the frontal turbulence arrest the frontogenesis?
3) How is the frontal turbulence maintained?

The contents of the paper are the following: the LES model is specified in section 2, the set of computational experiments in section 3, the front–turbulence decomposition and averaging of the flow fields and low-order moment

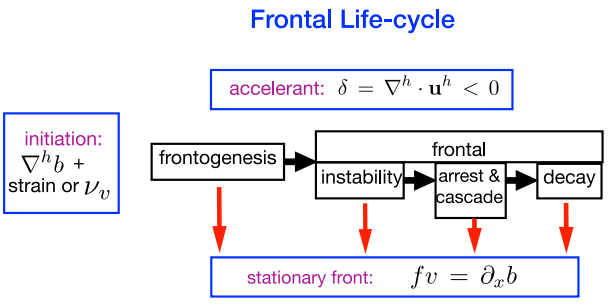

FIG. 1. A sketch of life cycle stages for a surface density front or filament (section 5).

dynamical balances in section 4, the analysis results in section 5 and its several subsections, and the summary in section 6. To a substantial degree the solutions are qualitatively similar in their spatial structure and temporal evolution across the control parameters M^2/f^2 and Q_*. Taking advantage of this, much of the presentation is focused on a particular case of strong M^2/f^2 and Q_* (called S100; see Table 1) at its time of peak frontal strength.

2. LES

The dynamics of the OBL, including submesoscale and boundary layer motions and frontogenetic turbulence, are assumed to be described by a conventional large-eddy simulation model for a high-Reynolds number Boussinesq flow with system rotation (Moeng 1984; McWilliams et al. 1997; Sullivan et al. 2007):

$$\frac{D\mathbf{u}}{Dt} = -\mathbf{f} \times \mathbf{u} - \nabla \pi + b\hat{\mathbf{z}} - \nabla \cdot \mathbf{T} \tag{2a}$$

$$\frac{D\theta}{Dt} = -\nabla \cdot \mathbf{C} \tag{2b}$$

$$\nabla \cdot \mathbf{u} = 0. \tag{2c}$$

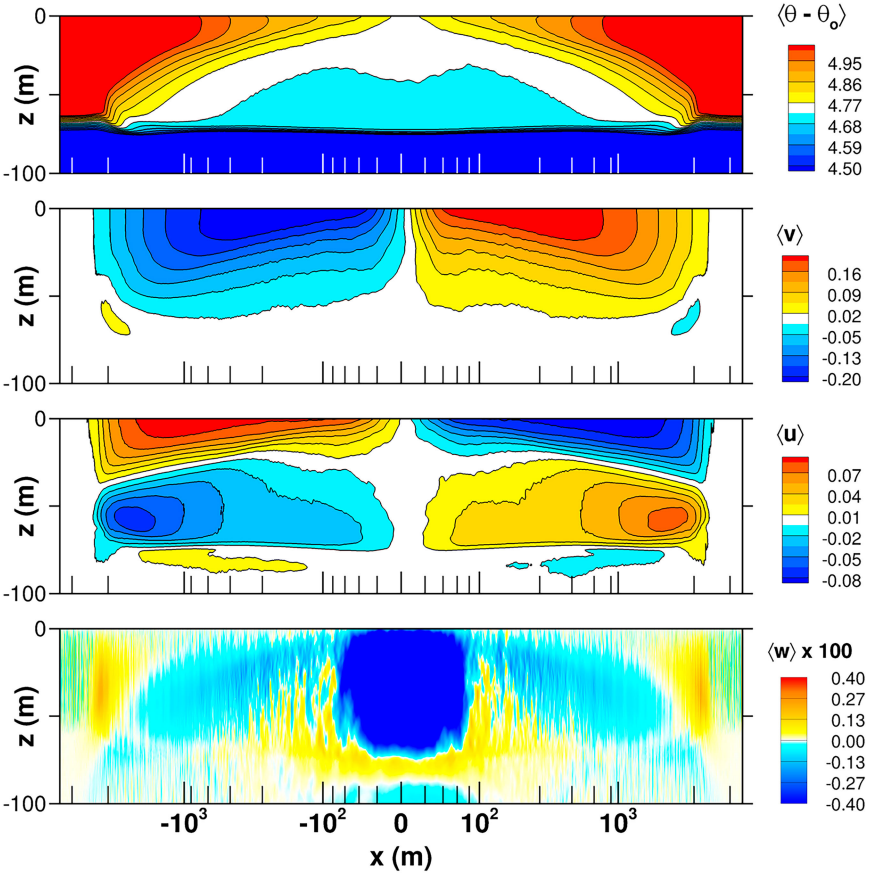

FIG. 2. Contours of average fields from case S100 at the time of peak frontal strength t_p from SM18. The velocity fields $\langle v, u, w \rangle$ and temperature difference $\langle \theta - \theta_o \rangle$ are in units of m s^{-1} and °C, respectively. The figure illustrates the sharp spatial changes with distance from the filament centerline. The x axis is logarithmic with minor tick marks located at intervals ±(20, 40, 60, 80) m, ±(200, 400, 600, 800) m, and ±(2000, 4000) m.

The LES model includes transport equations: (2a) for momentum $\rho\mathbf{u}$ and (2b) for temperature θ. The divergence free (incompressible) condition (2c) determines the elliptic pressure variable π. Variables that appear in (2) are Cartesian coordinates $\mathbf{x} \equiv x_i = (x, y, z)$, velocity components $\mathbf{u} \equiv u_i = (u, v, w)$, rotation vector $\mathbf{f} = (0, 0, f)$ with f the Coriolis parameter, and unit vector $\hat{\mathbf{z}}$ in the vertical direction z. The buoyancy variable is defined in terms of water density: $b = g(\rho_o - \rho)/\rho_o$ where ρ and ρ_o are density and reference density, respectively. We assume a linear equation of state connects temperature θ and density: $\rho = \rho_o[1 - \beta(\theta - \theta_o)]$ with β the coefficient of expansion and θ_o a reference temperature: $b = g\beta(\theta - \theta_o)$. Further details are given in SM18 and SM19. The coordinate directions (x, y, z) are also referred to as across-filament, along-filament, and vertical directions, respectively. The LES equations are formally derived by spatial filtering which introduces SGS momentum and scalar fluxes (**T**, **C**). These terms are modeled using standard eddy viscosity relationships $(\nu_t, \nu_c) \sim \sqrt{e}\ell$, where ℓ is a prescribed length scale proportional to the grid spacing Δ and the SGS energy e is the solution of a prognostic equation which includes advection, shear production, buoyancy production/destruction, diffusion, and a model of viscous dissipation ϵ, a concise review of the subgrid model is given by Moeng and Sullivan (2015).

Wave effects (McWilliams et al. 1997; Sullivan et al. 2007; McWilliams and Fox-Kemper 2013; Suzuki et al. 2016; McWilliams 2017, 2018; SM19) are omitted in the present work, although we know they can be relevant. The important new dynamics implicitly incorporated in (2) is additional forcing from a large-scale submesoscale cold dense filament. A pair of surface jets forms on either side of the imposed filament and their horizontal convergence is central to the TTW frontogenetic process that occurs inside the boundary layer. A related TTW problem using the K-profile parameterization scheme (Large et al. 1994), instead of LES, is described in McWilliams et al. (2015).

3. LES experiments

Our present LES database of oceanic frontal simulations consists of 16 cases. The database includes simulations with varying initial filament strength, surface forcing, surface waves, and orientation between wind-waves and the filament axis; a partial list of simulations is provided in SM18 and SM19. All simulations use a fine mesh of (8192, 3072, 256) grid points in a computational domain (x, y, z) of size (12, 4.5, −0.25) km; the mesh spacing $\Delta x = \Delta y = 1.46$ m and the stretched vertical grid has $\Delta z = [0.5–1.68]$ m with the finest vertical grid spacing near the water surface. The Coriolis parameter is $f = 0.781 \times 10^{-4}\ \mathrm{s}^{-1}$, the coefficient of expansion $\beta = 1.668 \times 10^{-4}\ ^\circ\mathrm{C}^{-1}$, and the reference temperature $\theta_o = 32.478^\circ$C. The simulations are transient and horizontally heterogeneous in x; the horizontal and vertical spatial structure of the 2D cold filament and the initialization procedure used in the simulations are described in SM18.

For the current analysis, we focus on simulations with no winds or waves and with surface cooling $Q_* = 15$ or 100 W m^{-2} and varying filament strength $M^2/f^2 = (10, 46, 84, 129)$, see (1) and Table 1. The initial filament horizontal scale $L = 2$ km is held constant, and changes in M^2 are the result of varying the initial amplitude of Δb. The analysis focuses on the time of peak frontal strength t_p, i.e., when the average vertical vorticity reaches a maximum. Diagnosed parameters in Table 1 include the Deardorff convective velocity scale $w_*^3 = \beta Q_* |h_i|/(\rho_o c_p)$ (where the initial OBL depth is $|h_i| \simeq 65$ m, and the ocean specific heat $c_p = 4.2 \times 10^3$ J kg^{-1} K^{-1}), the peak vertical vorticity ζ_{peak}, the peak turbulence kinetic energy $\mathrm{TKE}_{\mathrm{peak}}$ in the upper 5 m, the average horizontal width of the front l_w (defined later) at time t_p, and the vertical vorticity ζ_o at the initial time. The ζ_{peak} and $\mathrm{TKE}_{\mathrm{peak}}$ are normalized by their respective values at the initial time in the simulations to account for variations in M^2. The rest of the paper refers to the simulations by a case name in Table 1 defined by the combination of filament strength M^2 (strong, moderate, weak, very weak: S, M, W, VW) and the amount of imposed surface cooling $Q_* = 15$ or 100 W m^{-2}. SM18 and SM19 show that a frontal life cycle spans horizontal scales from the submesoscale $\mathcal{O}(10^4)$ m down to an arrest scale $\mathcal{O}(100)$ m and smaller. To present results over this range of scales, figures often use a double logarithmic x axis under the transformation $x_T = \mathrm{sign}(x)\log_{10}(|x|/c + 1)$ with $c = 50$ m where the horizontal range is $x \approx \pm[0–4 \times 10^3]$ m. Often figures are overlaid with x–z line contours of the mean thermal structure $\langle\theta - \theta_{\mathrm{ref}}\rangle$, where $\theta_{\mathrm{ref}} = 10^\circ$C.

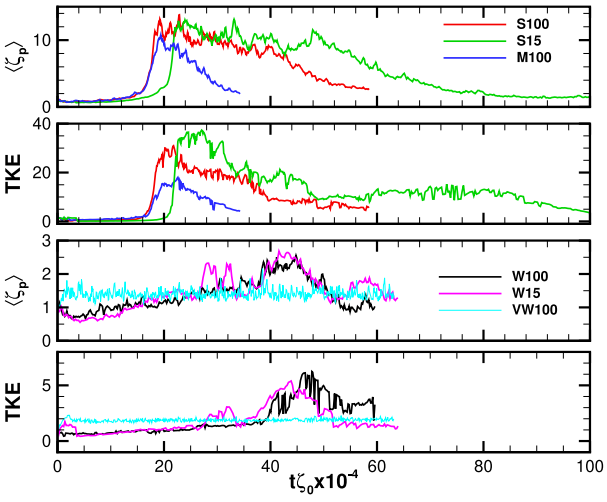

FIG. 3. Time variation of vertical vorticity and TKE with varying frontal strength M^2/f^2 and surface cooling Q_* (Table 1). To account for the variations in the filament initialization the vertical vorticity and TKE are normalized by their values at $t \sim 0$ for each simulation. The initialization recipe is described in SM18. The top two panels show results for strong and medium strength fronts (S15, S100, M100) in green, red, and blue lines, respectively, while the bottom two panels are results for weak and very weak strength fronts (W15, W100, VW100) in pink, black, and cyan lines, respectively. Note the range of the vertical axis changes between the top and bottom panels. The time axis is made dimensionless by ζ_o.

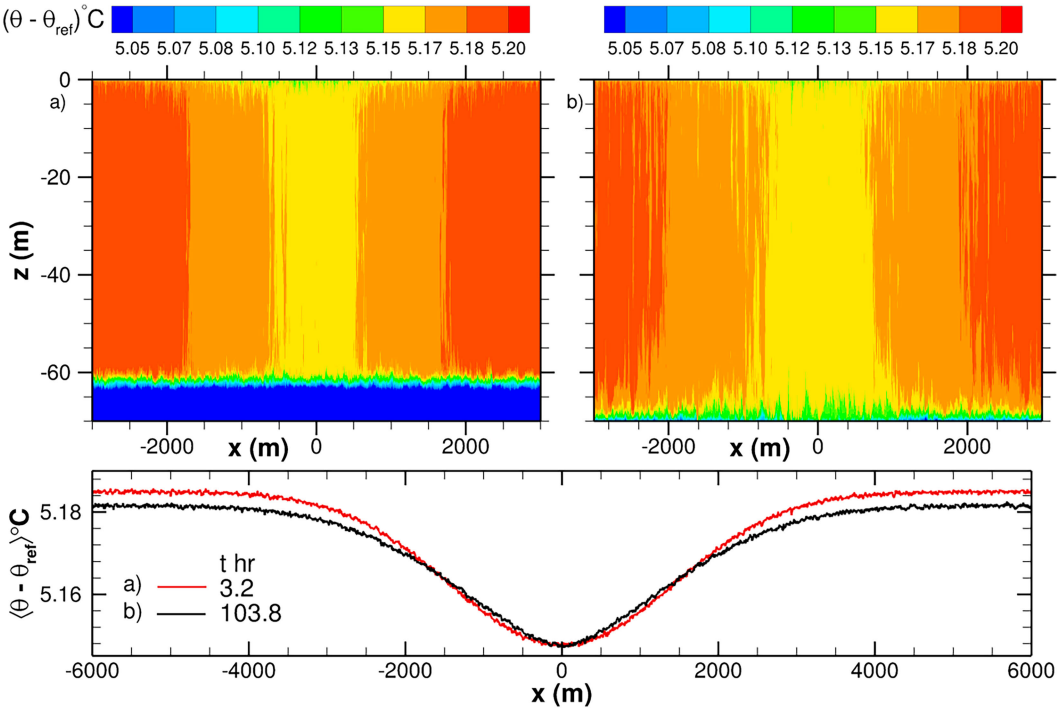

FIG. 4. Instantaneous temperature field $\langle \theta - \theta_{\text{ref}} \rangle$ in case VW100 at early and late times of 3.2 and 103.8 h, respectively. In the lower panel, line colors (red, black) denote the average temperature $\langle \theta - \theta_{\text{ref}} \rangle$ at early and late time at $z = 0$. A constant offset of 0.16°C is added to the temperature at the late time to highlight the comparison. The average temperature jump between the farfield and the filament centerline is 0.037° and 0.034°C at the early and late times, respectively. In case VW100 the bulk change in the OBL temperature with increasing time is mainly a consequence of surface cooling.

4. Averaging and moment balances

a. Flow decomposition

The flow is heterogeneous in the x–z directions; thus, to compute statistics we average in the statistically homogeneous y direction and over short time periods. At time t, any flow variable, say f or g, is decomposed into a mean and turbulent fluctuation

$$f(\mathbf{x}) = \langle f \rangle (x, z) + f'(\mathbf{x}), \tag{3}$$

where the angle bracket $\langle \cdot \rangle$ denotes a y average (i.e., an along-filament average) and a superscript prime $()'$ indicates a turbulent fluctuation. Average turbulent variances and fluxes are formed from the definitions

$$\langle f'f' \rangle = \langle ff \rangle - \langle f \rangle \langle f \rangle \text{ and } \langle f'g' \rangle = \langle fg \rangle - \langle f \rangle \langle g \rangle. \tag{4}$$

In general with winds and waves, the average $\langle f \rangle$ is the sum of a frontal perturbation that is the along-filament current and secondary circulation (which we combine into the abbreviation SC) plus a background average over an x–y plane (e.g., Hussain and Reynolds 1970; Sullivan et al. 2000). However, in the present study with uniform surface cooling and no surface wind the background averages are zero. Thus,

$$\langle f \rangle, \ \langle f \rangle \langle f \rangle, \text{ and } \langle f \rangle \langle g \rangle \tag{5}$$

define the mean, variance, and flux, respectively, of the SC; these statistical moments vary with (x, z, t). The exception to these rules is buoyancy (or temperature θ) where the background average over an x–y plane at each z, say $[\theta](z)$, is subtracted prior to computing its secondary circulation $\langle \theta \rangle$.

b. Low-order moment equations

For analysis purposes, we introduce the prognostic equation set for the y-averaged first-order moments $\langle u, v, w, \theta \rangle$ from SM18 with no surface wave effects:

$$\frac{\partial}{\partial t}\langle u \rangle = -\frac{\partial}{\partial x}(\langle u \rangle \langle u \rangle + \langle p \rangle + \langle u'u' + \tau_{uu} \rangle) - \frac{\partial}{\partial z}(\langle u \rangle \langle w \rangle + \langle u'w' + \tau_{uw} \rangle) + f\langle v \rangle \tag{6a}$$

$$\frac{\partial}{\partial t}\langle v \rangle = -\frac{\partial}{\partial x}(\langle u \rangle \langle v \rangle + \langle u'v' + \tau_{uv} \rangle) - \frac{\partial}{\partial z}(\langle v \rangle \langle w \rangle + \langle v'w' + \tau_{vw} \rangle) - f\langle u \rangle \tag{6b}$$

$$\frac{\partial}{\partial t}\langle w\rangle = -\frac{\partial}{\partial x}(\langle u\rangle\langle w\rangle + \langle u'w' + \tau_{uw}\rangle) + \left\langle \frac{g}{\theta_o}(\theta - \theta_o)\right\rangle - \frac{\partial}{\partial z}(\langle w\rangle\langle w\rangle + \langle p\rangle + \langle w'w' + \tau_{ww}\rangle) \tag{6c}$$

$$\frac{\partial}{\partial t}\langle \theta\rangle = -\frac{\partial}{\partial x}(\langle u\rangle\langle \theta\rangle + \langle u'\theta' + \tau_{u\theta}\rangle) - \frac{\partial}{\partial z}(\langle w\rangle\langle \theta\rangle + \langle w'\theta' + \tau_{w\theta}\rangle), \tag{6d}$$

where the right-hand side of each equation is written in flux conserving form. These expressions are specific to our problem posing, they are obtained by adopting a 2D density filament varying only in (x, z). In (6), the SGS fluxes for momentum (τ_{uu}, τ_{uv}, τ_{uw}, τ_{vw}, τ_{ww}) and for temperature ($\tau_{u\theta}$, $\tau_{w\theta}$) are parameterized using eddy viscosity prescriptions (e.g., Moeng and Sullivan 2015). For our simple equation of state $b = g\beta(\theta - \theta_o)$ and then (6d) can also be used to infer a buoyancy change.

c. Turbulence kinetic energy balance

The balance of terms in the turbulence kinetic energy (TKE) equation in frontogenesis is illuminating as it exposes the dependence on turbulence moments and mean current gradients. The TKE equation for resolved kinetic energy $q = u_i'u_i'/2$ is derived by straightforward steps (e.g., Tennekes and Lumley 1972) and in the current application contains additional terms owing to horizontal heterogeneity (Stull 1988, p. 124). The TKE equation is

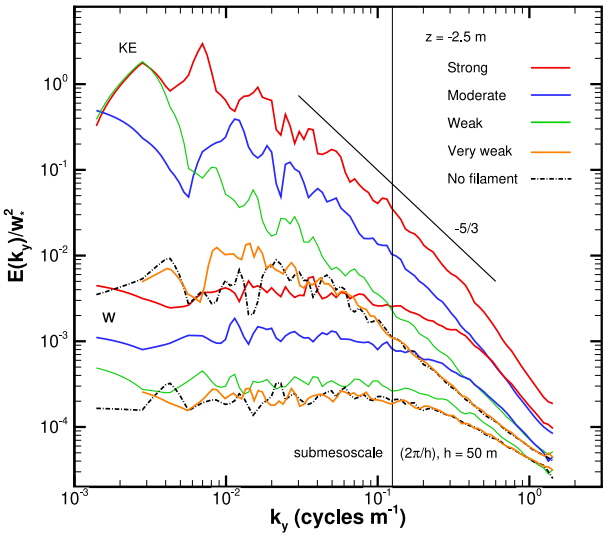

FIG. 5. Along-filament spectra averaged between $x = [-50, 50]$ m for simulations with strong S100, moderate M100, weak W100, and very weak VW100 filaments denoted by red, blue, green, orange colors, respectively, at t_p. The surface cooling $Q_* = 100\ \mathrm{W\,m^{-2}}$ in all these cases. The line groups show the spectra for the KE [the sum of the (u, v, w) spectra divided by 2] and for the vertical velocity, with some overlap that can be distinguished with the line coding. Spectra are computed near the water surface $z = -2.5$ m, and the normalization is by w_*^2. The vertical line at $k_y = 0.125\ \mathrm{m^{-1}}$ is an approximate boundary between submesoscale and boundary layer turbulence. The black dash–dot line shows the spectra for KE and w with no filament. The light black line indicates a spectral slope $\propto k_y^{-5/3}$.

$$\frac{\partial\langle q\rangle}{\partial t} = \underbrace{-\langle u\rangle\frac{\partial\langle q\rangle}{\partial x} - \langle w\rangle\frac{\partial\langle q\rangle}{\partial z}}_{A}\underbrace{- \frac{\partial}{\partial x}\langle u'(q + p')\rangle - \frac{\partial}{\partial z}\langle w'(q + p')\rangle}_{T}$$
$$\underbrace{-\langle u'^2\rangle\frac{\partial\langle u\rangle}{\partial x} - \langle u'v'\rangle\frac{\partial\langle v\rangle}{\partial x} - \langle u'w'\rangle\left(\frac{\partial\langle u\rangle}{\partial z} + \frac{\partial\langle w\rangle}{\partial x}\right) - \langle v'w'\rangle\frac{\partial\langle v\rangle}{\partial z} - \langle w'^2\rangle\frac{\partial\langle w\rangle}{\partial z}}_{S}$$
$$+ \underbrace{\beta\langle w'\theta'\rangle}_{B} \underbrace{- \langle\epsilon\rangle}_{D}. \tag{7}$$

As before, the operator $\langle\cdot\rangle$ indicates averaging in the homogeneous y direction at every x location. In (7) contributions from SGS terms are neglected except for the viscous dissipation ϵ. In crafting the viscous term we adopt the LES prescription

$$\epsilon = C_\epsilon\frac{e^{3/2}}{\ell}, \tag{8}$$

where $C_\epsilon \approx 0.93$, e is the SGS TKE, and ℓ is a stability corrected length scale (Moeng and Wyngaard 1988; Moeng and Sullivan 2015). The terms on the right-hand side of (7), identified by underbraces, are mean advection A, turbulent and pressure transport T, shear production of turbulence S, buoyancy B, and viscous dissipation D. Because of spatial heterogeneity, x and z variations both contribute to advection, transport, and shear production. Skyllingstad and Samelson (2020) and Taylor (2018) examine a TKE balance that is averaged over the x–y computational domain.

5. Results

A paradigm for the surface frontal life cycle is depicted in Fig. 1. Preexisting horizontal buoyancy gradients may become frontogenetic under the action of either a larger-scale strain flow or vertical momentum mixing due to a TTW secondary

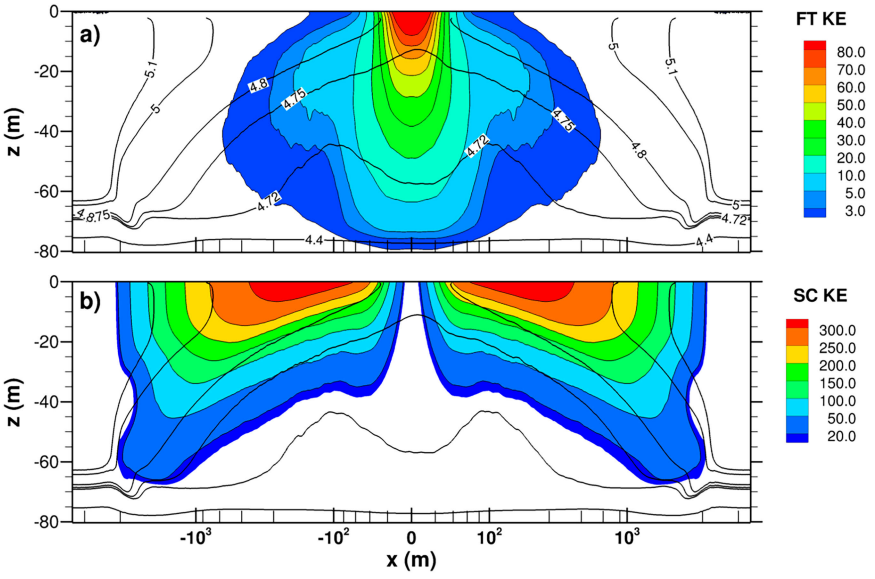

FIG. 6. Spatial distribution of (a) frontal turbulence kinetic energy (FT KE) and (b) secondary circulation kinetic energy (SC KE) at the time of peak frontal strength t_p from case S100. Notice the range of the color bar changes between the panels. Results are normalized by w_*^2. For reference, the panels are overlaid with identical line contours of the mean thermal structure $\langle \theta(x, z) - \theta_{\text{ref}} \rangle$ (°C).

circulation forced by air–sea momentum and buoyancy fluxes. At some point a frontal instability occurs with a growth rate that exceeds the frontogenetic rate. Frontal fluctuations amplify until their cross-frontal eddy momentum and/or buoyancy fluxes arrest the frontogenetic tendency at a finite frontal width. Meanwhile there is a forward kinetic energy cascade to small-scale frontal turbulence and dissipation. Thereafter these processes persist while the frontal system slowly decays or else the front is fragmented into frontal eddies. The frontal instability type and pattern of arresting eddy fluxes can differ depending on the frontal shape, air–sea fluxes, and Stokes drift influence from surface gravity waves. At any stage in this sequence, if the frontogenetic influences of strain and/or TTW abates and the air–sea fluxes and waves weaken, then the front (as indicated by the red arrows) can relax into a steady geostrophic balance between the horizontal buoyancy gradient and the alongfront flow, which itself might or might not be unstable to small perturbations.

In a more complex flow environment, these frontal processes may be overcome by disruptive advective tendencies that arrest the secondary-circulation's frontogenetic tendency. They can also be disrupted by energetic high-frequency motions, perhaps through shear dispersion (Young et al. 1982; Wenegrat et al. 2020), or overcome by very strong turbulent mixing (Young 1994; Crowe and Taylor 2018; Bodner et al. 2020). In our set of simulations, we make contact with the latter effect when the initial frontal strength is very weak with strong convection (i.e., case VW100 in Table 1). Our view is that the sequence in Fig. 1 is common in the ocean but not universal.

The conception here of a frontal life cycle is suitable for a statistically homogeneous midocean environment; in that sense it is quite different from the paradigm of embedded weather fronts in atmospheric cyclonic storms (e.g., Thorncroft et al. 1993).

a. *Dependencies on M^2 and Q_**

The LES simulations broadly follow the frontal life cycle outlined in Fig. 1 of frontogenesis, fluctuation growth, arrest, and slow decay. The visualization in Fig. 2, at $t = t_p$, depicts specific frontogenetic signatures in case S100: viz., a pair of v jets of opposite sign straddle a sharp temperature (density) front of finite width ≃100 m, secondary circulations in $\langle u \rangle$ (converge, diverge) at the (top, bottom) of the OBL, and the vertical velocity $\langle w \rangle$ strongly downwells at the filament centerline.

The details of the life cycle and flow patterns (e.g., Fig. 2) of each LES experiment differ somewhat depending on input parameters. Inspection of Fig. 3 and Table 1 shows that the initial filament strength M^2 impacts the temporal evolution of frontogenesis, the amplitude of the secondary circulations, the filament arrest width ℓ_w, and the frontal turbulence. With fixed M^2, varying the initial turbulence level set by the surface cooling, however, plays a smaller role in CFF at least over the range $Q_* = [15\text{–}100]\,\mathrm{W\,m^{-2}}$. Increasing filament strength shortens the time to peak frontal strength by nearly 30 h (≈30×10^4 in $t\zeta_o$ units), seen by comparing the results for cases S100 and W100 with $M^2/f^2 = (128, 46)$, respectively. Filament strength increases and sharpens the peak vertical vorticity and also enhances $\mathrm{TKE}_{\mathrm{peak}}$ near the water surface. The frontal width ℓ_w varies inversely with filament strength M^2. The decay stage of

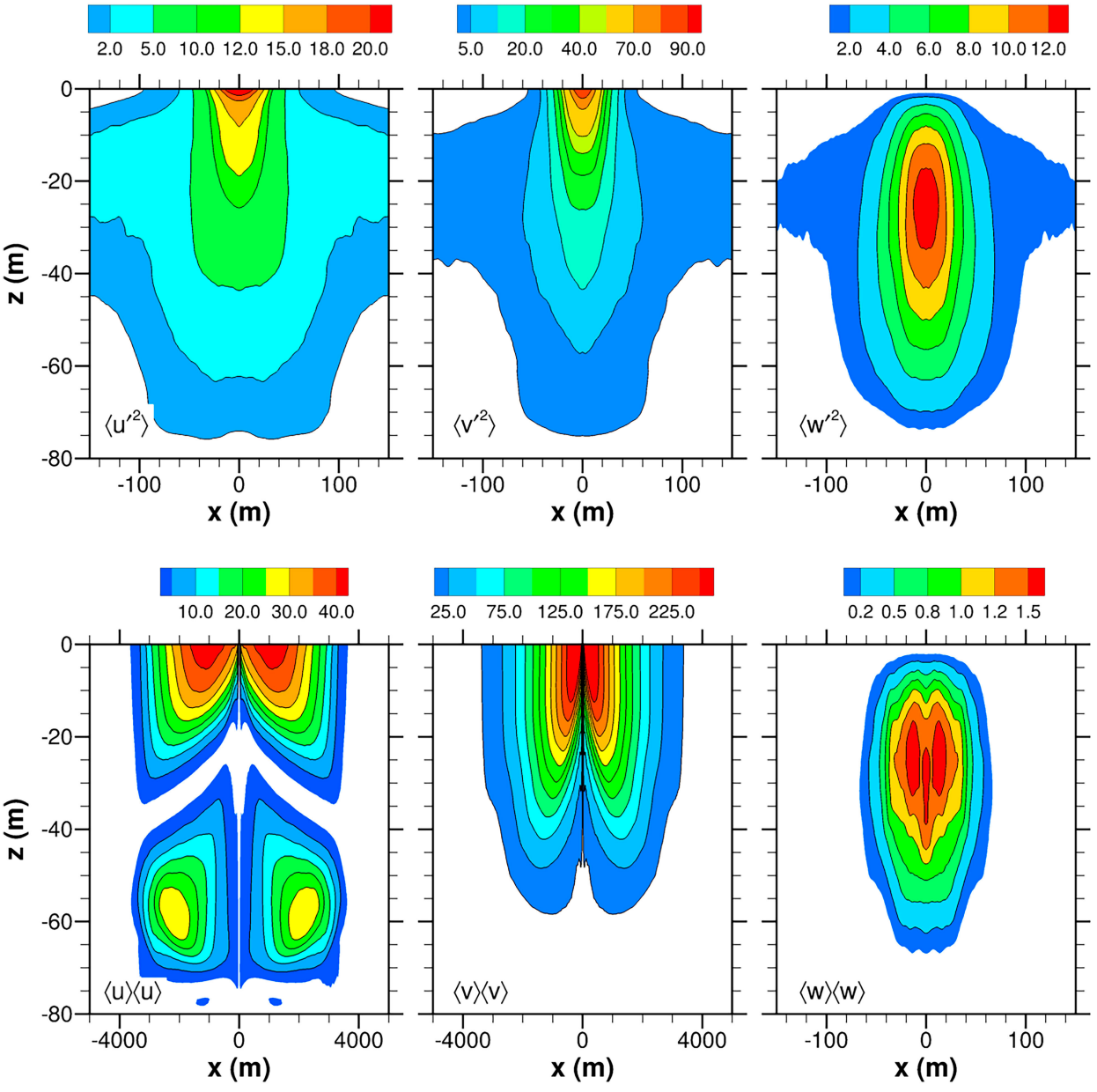

FIG. 7. Momentum variances at the time of peak frontal strength t_p from case S100. (top) Turbulence variances $\langle u'^2, v'^2, w'^2 \rangle$ and (bottom) SC variances $\langle u \rangle^2$, $\langle v \rangle^2$, $\langle w \rangle^2$. Notice the range of the color bar and the width of the x axis change between the panels. Variances are normalized by w_*^2.

case S15 is an exception; visualization shows the filament tends to modestly rotate in the x–y plane, and thus averaging in y at constant x intermittently crosses the filament axis producing the oscillating TKE decay shown in the bottom panel of Fig. 3. We find that the combination of weak cooling and weak filaments, e.g., case W15 in Table 1, leads to complex flow patterns as the seeds of frontogenesis gradually disappear.

The sole exception in our dataset is that a frontal life cycle is not triggered in case VW100 over the time period $0 < t < 90$ h, even though the filament structure in $\langle \theta \rangle(x, z)$ and in the secondary circulation persists throughout this integration period. Case VW100 has a high level of background turbulence but very weak geostrophic jets, more than 10 times smaller than case S100, at $t = 0$. Flow visualization of the temperature field in VW100 at early and late times shows bulk cooling of the OBL. Temperature anomalies, geostrophic jets, and the SC in u can be identified at late time but are only slightly weaker compared to their initial values. The temperature jump between the farfield and the filament centerline is 0.037° and 0.035°C at early and late times, respectively, and the filament width increases slightly (Fig. 4). The change in the OBL temperature field is

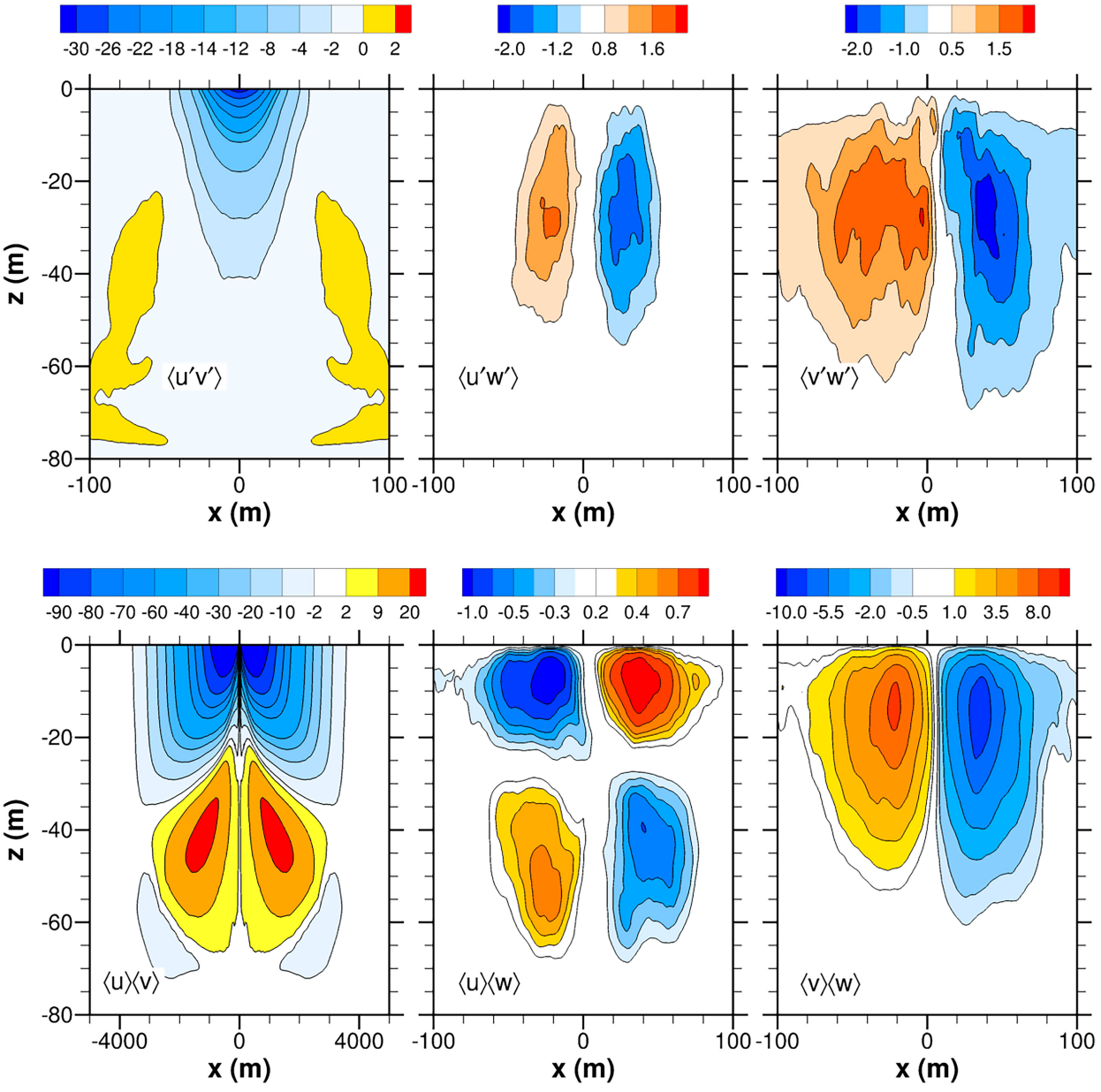

FIG. 8. Momentum fluxes at the time of peak frontal strength t_p from case S100 for comparison with Fig. 7. (top) Turbulence fluxes $\langle u'v', u'w', v'w' \rangle$ and (bottom) SC fluxes $\langle u \rangle \langle v \rangle$, $\langle u \rangle \langle w \rangle$, $\langle v \rangle \langle w \rangle$. Notice the range of the color bar and the width of the x axis change between the panels. Fluxes are normalized by w_*^2.

mainly due to surface cooling not frontogenesis. OBL turbulence generated by surface cooling appears to quench the frontogenetic triggers for this very weak filament, a result broadly similar to the findings described by Kaminski and Smyth (2019) for a modified Kelvin–Helmholtz instability in a preexisting turbulent flow. We conclude that sufficiently strong turbulence or weak initial filament strength leads to slow frontolysis by vertical shear dispersion in combination with vertical buoyancy mixing, as suggested in Young (1994) and Crowe and Taylor (2018, 2019), dominating any advective frontogenesis by the secondary circulation. At the other extreme, in the absence of background turbulence the filament flow simply tends to be in a steady-state geostrophic balance. Nevertheless, over the wide range of control parameters explored here, except for case VW100, the frontal life cycle does occur approximately as indicated in Fig. 1.

The along-filament (y) 1D power spectra of the turbulence kinetic energy and the vertical velocity from cases S100, M100, and W100 are depicted in Fig. 5; the smoothed spectra are constructed from the turbulence u_i', and they are averaged over individual along-filament spectra within the range $x = [-50, 50]$ m near the water surface. These spectra illustrate a greatly increased

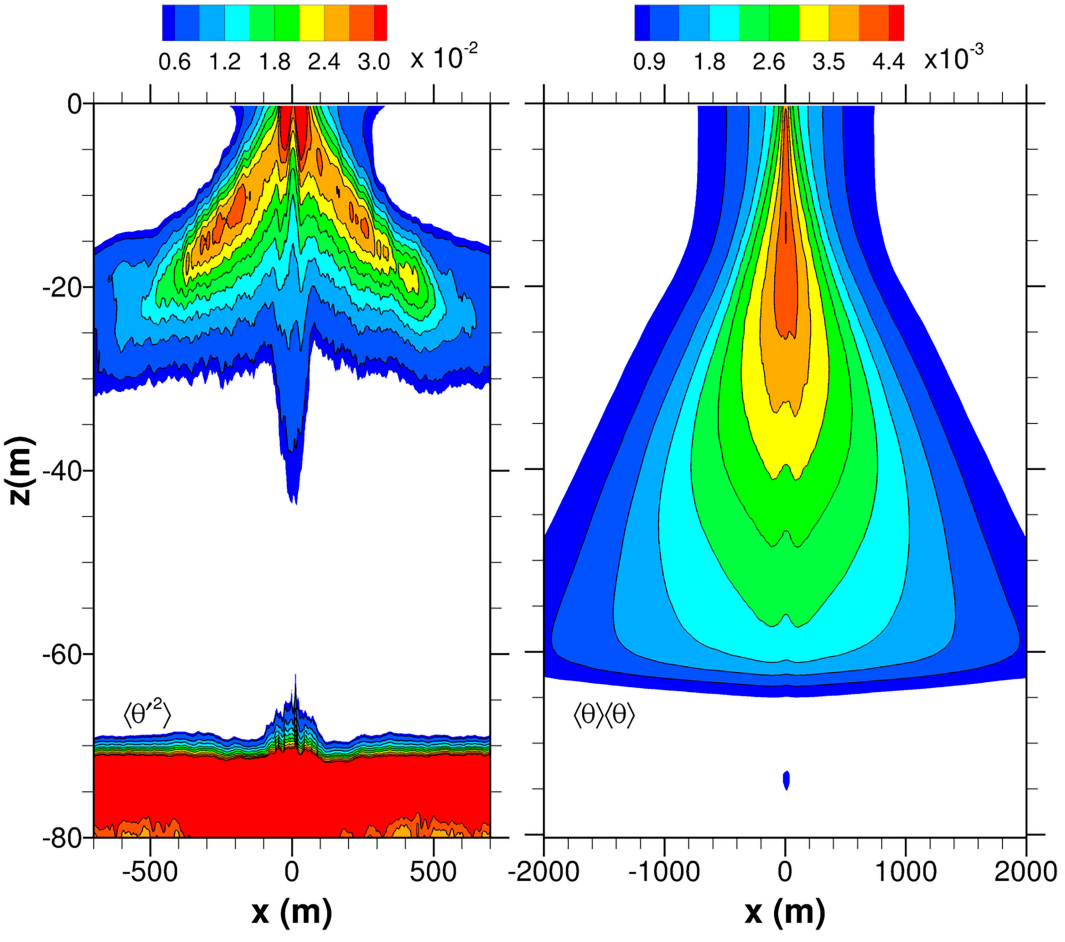

FIG. 9. Temperature variances at the time of peak frontal strength t_p from case S100. (left) Turbulence temperature variance $\langle\theta'^2\rangle$ and (right) SC temperature variance $\langle\theta\rangle^2$. Notice the range of the x axis and the color bar changes between the panels. Variances are normalized by $(Q_*/w_*)^2$.

energy level at all wavenumbers k_y at the time of peak frontal strength, compared to a simulation without an initial filament. The energy increase depends on M^2 as anticipated from the $\mathrm{TKE}_{\mathrm{peak}}$ in Fig. 3. At $z = -2.5$ m, the spectra also hint that the near surface turbulence is highly anisotropic based on a comparison of the (high, low) spectral levels of kinetic energy and vertical velocity, respectively; they become more nearly isotropic at large k_y in the boundary layer interior. Note the smooth continuous variation in spectral levels for wavenumbers $k_y \approx 2\pi/|h|$ crossing between the submesoscale and boundary layer regimes. At high wavenumbers the KE spectra are displaced vertically depending on M^2 but have approximately the same slope $\propto k_y^{-5/3}$ over a broad range of scales in the frontal zone. In unforced simulations, Verma et al. (2019) find a slope change from -3 to $-5/3$ at a scale $\mathcal{O}(100)$ m with the spectra averaged over a width of 2.4 km. Spectra of KE with no filament are more than two orders in magnitude smaller at low wavenumbers compared to the simulations with a strong filament. Frontogenesis increases the energy level, in particular the energy in the horizontal turbulence, indicative of a forward energy cascade from the submesoscale to dissipation, also see section 5f.

b. Kinetic energy, variances, and fluxes

Turbulence in CFF is markedly different than its counterpart in a horizontally homogeneous boundary layer driven by surface cooling because of the organized SC flow. This is illustrated in Figs. 6–8, which depict low-order moments from case S100, viz., kinetic energy, horizontal and vertical variances, and fluxes of momentum. Turbulence and SC statistics are shown separately in the top and bottom panels, and all fields are made dimensionless by the convective velocity w_*^2.

The frontal turbulence kinetic energy $\langle u_i' u_i'/2\rangle$ (FT KE) and the secondary circulation kinetic energy $\langle u_i\rangle\langle u_i\rangle/2$ (SC KE) are compared in Fig. 6. FT and SC KE values are similar in magnitude but feature key differences. FT KE is localized on the filament centerline while the SC KE peaks outside of the filament zone, near $x \approx \pm 300$ m and is spread over hundreds of meters horizontally. There is a noticeable and mandatory void in the SC KE at $x = 0$ where $\langle u, v\rangle$ change signs.

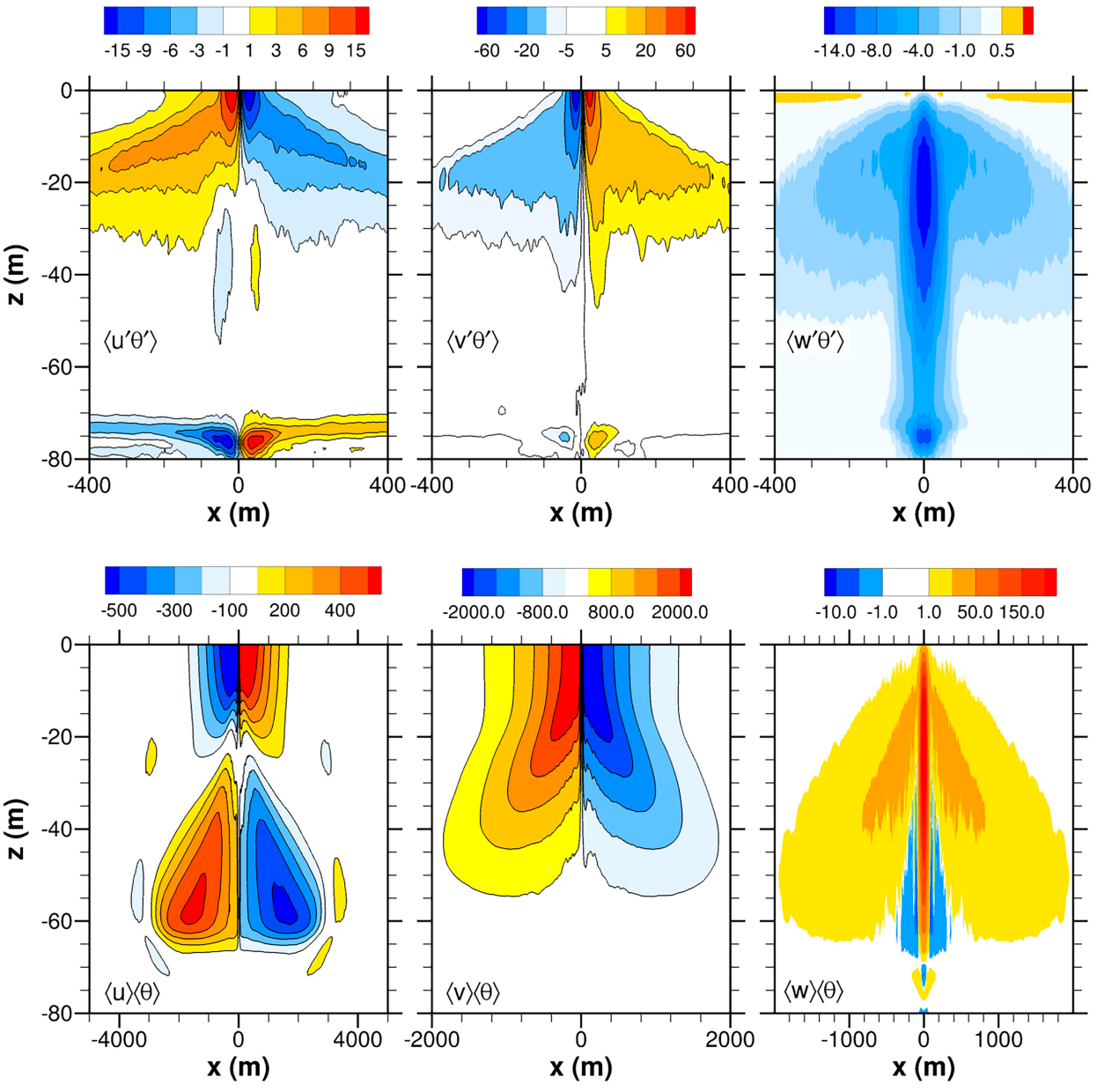

FIG. 10. Temperature fluxes at the time of peak frontal strength t_p from case S100. (top) Turbulence temperature fluxes $\langle u'\theta', v'\theta', w'\theta'\rangle$ and (bottom) SC temperature fluxes $\langle u, v, w\rangle\langle\theta\rangle$. Notice the range of the color bar changes between the panels. Fluxes are normalized by surface cooling Q_*.

Individual variances and fluxes highlight the fundamental role of horizontal turbulence in CFF. Near the front centerline there are large near surface peaks in $\langle u'^2, v'^2, u'v'\rangle$, interior positive and negative peaks in $\langle u'w', v'w'\rangle$, and a large peak in vertical velocity variance $\langle w'^2\rangle$. For comparison, the maximum $\langle w'^2\rangle/w_*^2 \approx 0.45$ in a horizontally homogeneous convective atmospheric boundary layer (e.g., Sullivan et al. 2014); in CFF $\langle w'^2\rangle/w_*^2 > 10$ beneath the downwelling jet. The across-filament gradients in $\langle u, v\rangle$ generate large horizontal turbulent fluctuations (u', v'), and thus large variances $\langle u'^2, v'^2\rangle$. CFF also generates momentum fluxes, and in particular a large negative horizontal momentum flux $\langle u'v'\rangle/w_*^2 \approx -30$ at the water surface; horizontal and vertical momentum fluxes are near zero in the homogeneous convective boundary layer. The nonzero vertical momentum fluxes $\langle u'w', v'w'\rangle$ are key ingredients in boundary layer induced frontogenesis: their vertical divergence initiates the SC, and they contribute to a turbulent thermal wind balance (TTW) (Gula et al. 2014; McWilliams et al. 2015). Vertical momentum fluxes are nonzero in an OBL with a submesoscale filament even when

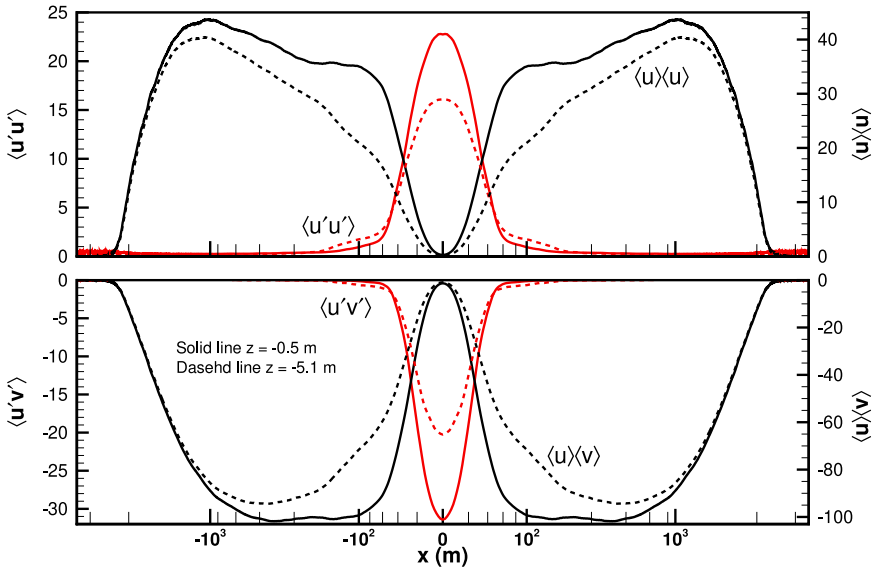

FIG. 11. (top) Variation of turbulence and SC horizontal variances ($\langle u'u'\rangle$, $\langle u\rangle^2$) and (bottom) horizontal flux ($\langle u'v'\rangle$, $\langle u\rangle\langle v\rangle$) at t_p, slicing perpendicular to the axis of the geostrophic jets. Results are shown at $z = (-0.5, 5.1)$ m indicated by solid and dashed lines, respectively. The horizontal divergence of these terms appears on the right-hand side of the tendency equations (6a) and (6b) for $\partial_t\langle u, v\rangle$. The x axis is logarithmic with minor tick marks located at intervals $\pm(20, 40, 60, 80)$ m, $\pm(200, 400, 600, 800)$ m, and $\pm(2000, 4000)$ m. Variables on the y axis are normalized by w_*^2.

turbulence in the farfield is driven solely by surface cooling, i.e., with no surface winds SM18. Broadly, submesoscale filaments and frontogenesis can generate powerful horizontal and vertical turbulent motions much greater than those found in homogeneous OBLS with comparable surface forcing.

The amplitude and spatial organization of the SC variances and fluxes provide an interesting contrast to their turbulence counterparts. The SC momentum variances $\langle u\rangle^2$, $\langle v\rangle^2$, and $\langle w\rangle^2$ and fluxes $\langle u\rangle\langle v\rangle$, $\langle u\rangle\langle w\rangle$, and $\langle v\rangle\langle w\rangle$ are depicted in the lower panels of Figs. 7 and 8, respectively. The fine-resolution large-domain LES captures the broadband spectrum of motions in CFF. The peak turbulence levels are mainly confined to a narrow frontal zone $[-100 < \ell < 100]$ m, while outside of the frontal zone turbulence decays rapidly as it asymptotes to its farfield state. Broadly, the SC variances are larger than their turbulence counterparts, but are spread over much larger horizontal distances on the order of kilometers. The notable exception is vertical velocity variance, where $\langle w'^2\rangle \approx 10\langle w\rangle^2$ at the front centerline, i.e., downwelling is dominated by turbulence not by SC variance $\langle w\rangle^2$, which is potentially important for transport from the oceanic surface to the interior (Freilich and Mahadevan 2022; Capó and McWilliams 2022; Aravind et al. 2023). The momentum flux patterns reflect the direction and magnitude of the SC and the geostrophic jets in the filament. The jet velocity $\langle v\rangle$ is (negative, positive) on the (left, right) side of the front while the (upper, lower) branches of $\langle u\rangle$ are (converging, diverging), see Fig. 2 and SM18. Coupling between the cross-frontal SC and the filament jets generates a large negative horizontal momentum flux $\langle u\rangle\langle v\rangle/w_*^2 \sim -90$ in the upper OBL. By comparison $\langle u\rangle\langle v\rangle/w_*^2 \sim 10$ in the lower OBL. The vertical momentum fluxes $\langle u\rangle\langle w\rangle$, $\langle v\rangle\langle w\rangle$ are notably smaller than the horizontal momentum flux due to the weak downwelling $\langle w\rangle$.

The turbulence and the SC are closely coupled to the buoyancy (temperature) field. Temperature variances and fluxes are shown in Figs. 9 and 10; turbulence fluxes $\langle u'\theta', v'\theta', w'\theta'\rangle$ and SC fluxes $\langle u, v, w\rangle\langle\theta\rangle$ are depicted in the top and bottom panels, and all fields are normalized by the surface cooling Q_*. Notice the sign of the temperature fluxes are reversed between the turbulence and SC fields, also all fluxes are greater in magnitude compared to Q_*, i.e., submesoscale dynamics dominate the background boundary layer convection. Similar to momentum, the SC fluxes are larger in amplitude and spread over greater horizontal distances compared to their turbulence counterparts. The vertical temperature flux is again special with $\langle w\rangle\langle\theta\rangle$ opposite in sign and greater in magnitude than $\langle w'\theta'\rangle$ especially near the front centerline. The horizontal SC temperature flux shows upper and lower lobes with opposite signs because of the SC. The horizontal convergence, $-\partial_x$, of the SC and turbulence fluxes are opposite in sign, and near the surface the competition leads to warming $\partial_t\langle\theta\rangle > 0$, while the return leg of the SC at the bottom of the layer leads to cooling $\partial_t\langle\theta\rangle > 0$, see section 5e.

c. *Frontal arrest*

The dynamics of frontal arrest are still in a state of discovery and likely depend on the background forcing and turbulence.

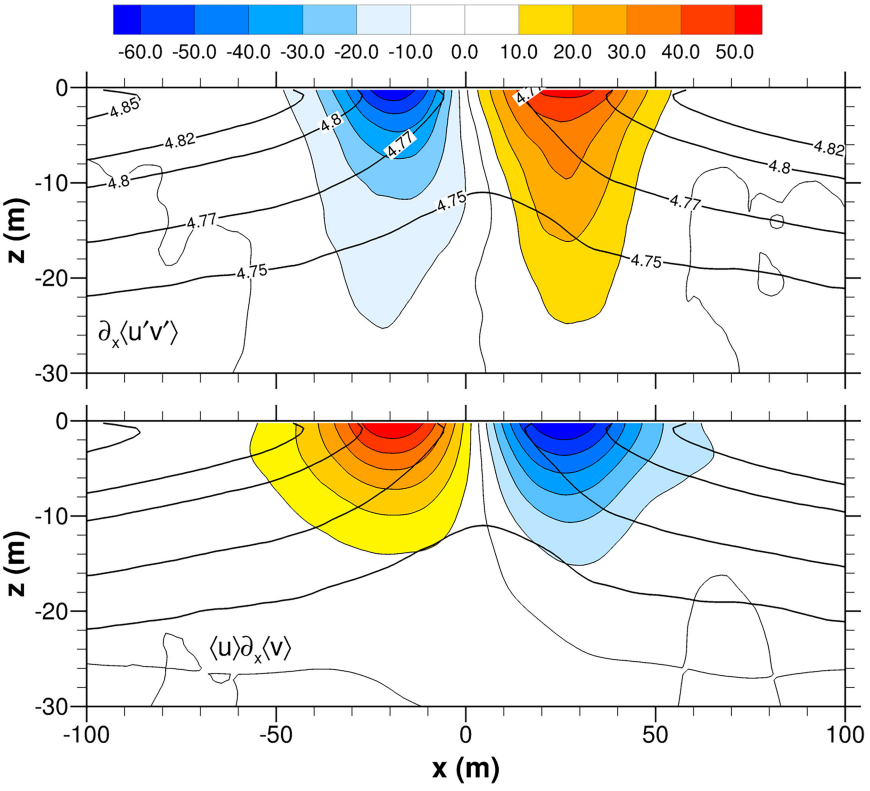

FIG. 12. Comparison of the (top) turbulence flux divergence $\partial_x\langle u'v'\rangle$ and (bottom) SC advection $\langle u\rangle\partial_x\langle v\rangle$ at the time of peak vertical vorticity t_p from case S100. This is the primary balance in the along-filament momentum equation (6b). Terms are normalized by $w_*^2/|h_i|$. The panels are overlaid with identical line contours of the mean thermal structure $\langle\theta(x, z) - \theta_{\text{ref}}\rangle$ (°C).

For example, Samelson and Skyllingstad (2016) state that the Kelvin–Helmholtz instability is the primary arrest mechanism for laminar fronts as predicted by Hoskins and Bretherton (1972). Based on a scale analysis, Snyder (1998) finds that the atmospheric boundary layer impacts fronts and horizontal advection, and in general the boundary layer cannot be ignored. Analysis of our fine-resolution LES that evolve from a initially turbulent state suggests an alternative mechanism. In our flow where a submesoscale front evolves in a fully turbulent OBL, an across-filament (lateral) shear instability is the most likely mechanism that produces ingredients leading to frontal arrest McWilliams et al. (2015), SM18, and SM19. In the y-averaged equations, the horizontal divergence ∂_x of the variances and fluxes reflects this arrest mechanism as shown in Fig. 11. Notice in the frontal zone the slopes of the SC horizontal variance and flux are opposite in sign compared to their turbulence counterparts. In (6b), $-\partial_x\langle u'v'\rangle$ tends to weaken the filament jets while $-\partial_x\langle u\rangle\langle v\rangle$ strengthens the jets. Frontal arrest in the v momentum equation occurs when the horizontal turbulent flux increases sufficiently to balance the SC advection, i.e., the approximate balance $\langle u\rangle\partial_x\langle v\rangle \approx \partial_x\langle u'v'\rangle$ as shown in Fig. 12. Also, arrest mechanics are in (6a). In the frontal zone $-\partial_x\langle u'u'\rangle$ and $-\partial_x\langle u\rangle^2$ (weaken, strengthen) the flow tendency $\partial_t\langle u\rangle$. Thus, turbulence plays a key double role in boundary layer induced frontogenesis: it initiates the SC through vertical momentum fluxes, while horizontal turbulence variance and flux act to promote frontal arrest. The largest turbulence variance $\langle v'^2\rangle$ does not explicitly appear in (6). Based on the results in Fig. 12, horizontal turbulent flux provides a good measure of the final arrest width, i.e., we define the arrest width l_w as the distance from the centerline where the flux divergence $\partial_x\langle u'v'\rangle$ first falls to zero outside of the filament zone, and $l_w \propto 1/M^2$; see Table 1.

d. TKE balance

Vertical profiles of the TKE terms at the time of peak frontal strength t_p in case S100 at selected x locations far from and near the front centerline are shown in Fig. 13. The contours in Fig. 14 provide an x–z view of the sharp spatial changes in TKE terms. The profiles and contours illustrate significant structural changes in the boundary layer and the shifting balance in TKE production and destruction under frontogenesis. In the farfield left of the front centerline $x \simeq -6$ km (Fig. 13), the primary balance is between buoyant production and dissipation with the turbulent and pressure transport playing a lesser role in rearranging TKE in the vertical. This balance in the upper ocean is a familiar one based on similar results for a highly convective atmospheric boundary layer (e.g., Moeng and Wyngaard 1988). The vertical and

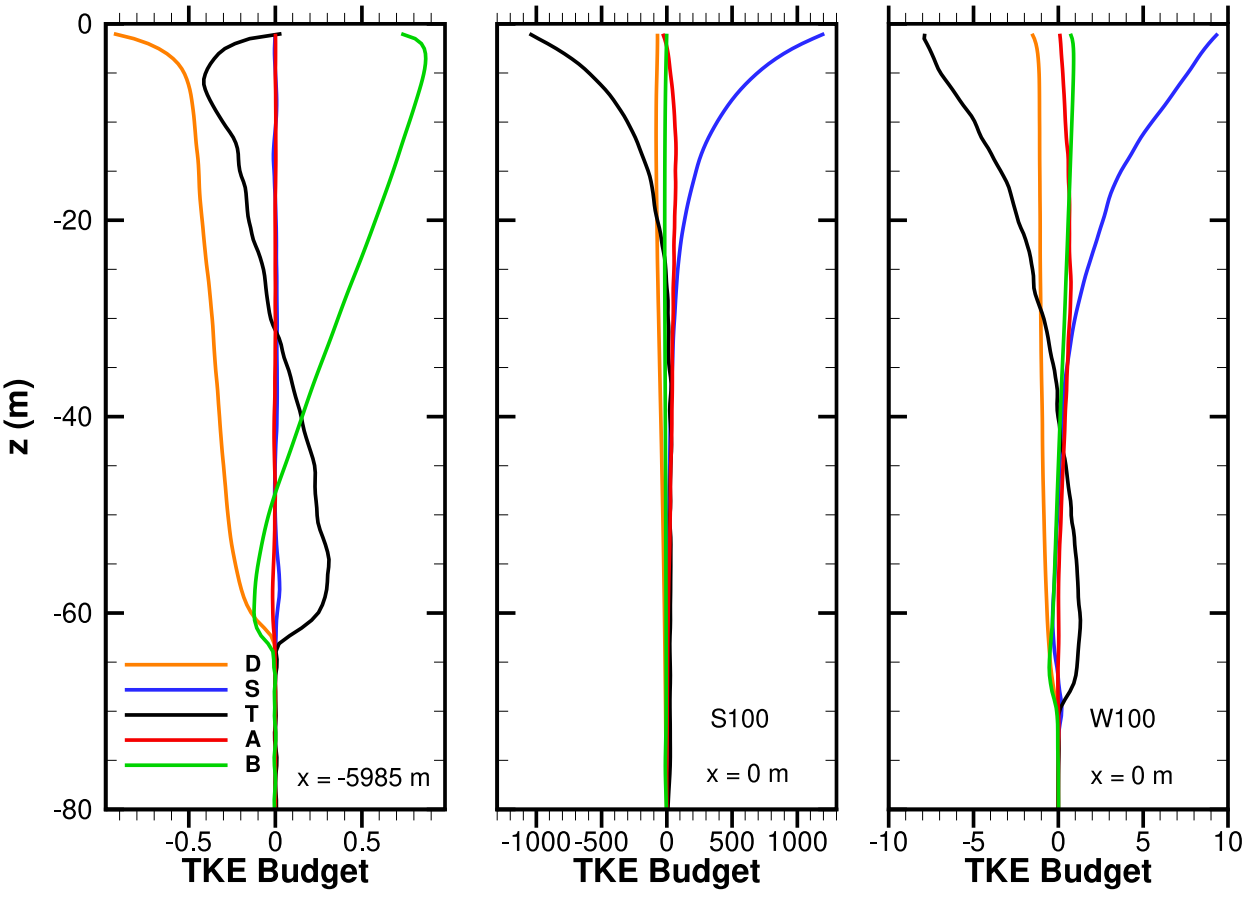

FIG. 13. Vertical profiles of terms in the TKE balance (7) at locations $x = [-5985, 0]$ m far from and at the front centerline at t_p. (left) Balance in the farfield and balance at front centerline (center) from case S100 and (right) from case W100. TKE terms (dissipation D, shear production S, transport T, advection A, buoyancy B) are denoted by colored lines (orange, blue, black, red, and green, respectively). All terms are normalized by $w_*^3/|h_i|$, and the range of the x axis changes between the panels.

horizontal structure of the TKE balance shifts under the action of CFF. In CFF the horizontal legs of the secondary circulations at the top and bottom of the boundary layer promote turbulence shear production, and they transport warm and cool water. At the top of the layer, the SC horizontal convergence collapses the horizontal distance between the geostrophic jets, thus further increasing mean gradients, $\partial_x\langle u, v\rangle$.

For a convective boundary layer, turbulence production changes in CFF. In the farfield away from the front, turbulence is mainly produced by buoyancy, but near the front centerline, $-200 < x < 200$ m, shear production grows and becomes the dominant TKE source (Figs. 13 and 14). Meanwhile buoyancy reverses sign and becomes a weak sink; recall surface cooling is constant with x (note the yellow contours in the top panel of Fig. 14), and thus the reversal of buoyancy's role in the interior of the boundary layer is a consequence of frontogenesis.

Decomposition of the shear production S in (7) into vertical S_v and horizontal S_h contributions,

$$S_v = -\langle u'w'\rangle\langle \partial_z u + \partial_x w\rangle - \langle v'w'\rangle\langle \partial_z v\rangle - \langle w'w'\rangle\langle \partial_z w\rangle, \tag{9a}$$

$$S_h = -\langle u'u'\rangle\partial_x\langle u\rangle - \langle u'v'\rangle\partial_x\langle v\rangle, \tag{9b}$$

illustrates important differences compared to a horizontally homogeneous boundary layer with only vertical shear; the spatial variation of S_v and S_h in the frontal zone are shown in Fig. 15. At the centerline $x = 0$, S_v features a sign change $S_v < 0$ for $-20 < z < 0$ m while $S_v > 0$ for $z < -20$ m. The gradient $\langle \partial_z w\rangle > 0$ is responsible for the negative values of S_v along $x = 0$, also see the w variance in the right panel of Fig. 7. Meanwhile S_h reaches a maximum near the water surface. Notice the vertical production term $-\langle u'w'\rangle\langle \partial_z u + \partial_x w\rangle$ is smaller than $-\langle v'w'\rangle\langle \partial_z v\rangle$.

The horizontal production term $-\langle u'v'\rangle\partial_x\langle v\rangle > 0$ is the dominant source of TKE with $-\langle u'u'\rangle\partial_x\langle u\rangle < 0$ playing a smaller role; note the latter term is positive since the SC switches sign crossing the front centerline, i.e., $\langle \partial_x u\rangle < 0$. Hefty values of S_h are consistent with the development of a

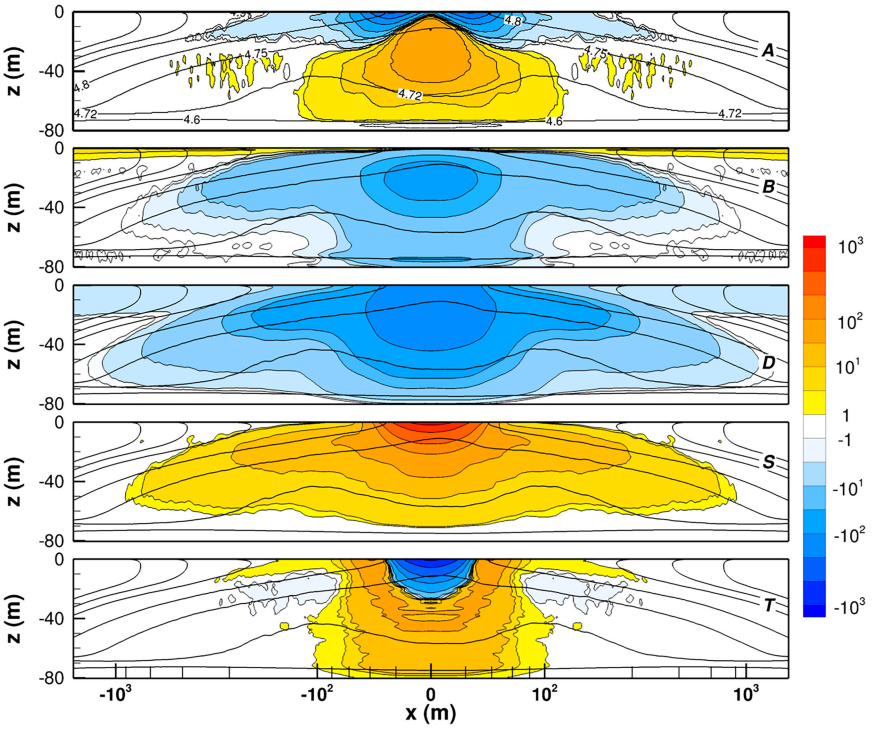

FIG. 14. Spatial variation of the terms in the TKE balance (7) in an x–z plane from case S100: advection A, buoyancy B, dissipation D, shear production S, and transport T, are shown from top to bottom, respectively, at t_p. All terms are normalized by $w_*^3/|h_i|$, and the x axis is logarithmic with minor tick marks located at intervals $\pm(20, 40, 60, 80)$ m and $\pm(200, 400, 600, 800)$ m. The heavy contour lines in each panel are the mean thermal structure $\langle \theta - \theta_{\text{ref}} \rangle$ (°C).

lateral shear instability, a large horizontal surface flux $-\langle u'v' \rangle$, large variances $\langle u'^2, v'^2 \rangle$, and steep horizontal gradients ($\partial_x \langle v \rangle > 0$, $\partial_x \langle u \rangle < 0$) in filament frontogenesis (SM18; SM19). Moving away from the centerline S_h decays rapidly while S_v features a sign change near $z \simeq -20$ m. Near the filament centerline horizontal production of TKE exceeds vertical production, but both terms fall off rapidly in the farfield $|x| > 1000$ m with S_h decaying more rapidly than S_v. Both terms are nearly zero as expected for convective driven turbulence at $|x| = 6000$ m.

An important and unexpected property of the TKE balance is shown in the center and right panels of Fig. 13 and the bottom panel of Fig. 14. At the front centerline $x = 0$, turbulent transport T, not dissipation D, balances the large shear production S. This balance holds for all values of M^2/f^2 considered in our study, i.e., for strong and weak filaments. Decomposition of T into its vertical and horizontal components is shown in the top and bottom panels of Fig. 16. Near the water surface both transport terms are negative, acting to balance S, but the horizontal transport reverses sign at the edges of the frontal zone. Further decomposition of the transport terms shows the third-order moments $\langle u'q^2, w'q^2 \rangle$ are larger than their pressure counterparts $\langle u'p', w'p' \rangle$ (not shown). Near the front centerline, dissipation is large compared to the farfield, but the high level of TKE generated by horizontal shear $\partial x \langle v \rangle$ is mainly balanced by horizontal and vertical TKE transport away from the front by third-order turbulence and pressure moments, i.e., nonlocal effects are dominate at the filament centerline. Further examination of T (section 5g) shows that the third-order moments are modestly correlated with horizontal and vertical derivatives of the TKE, i.e., the moments are approximately a downgradient process

$$\langle u'(q + p') \rangle \approx -\mu_h(x, z) \frac{\partial}{\partial x} \langle q \rangle \quad \text{and}$$

$$\langle w'(q + p') \rangle \approx -\mu_v(x, z) \frac{\partial}{\partial z} \langle q \rangle \,. \tag{10}$$

Thus, (10) implies the horizontal and vertical transports T roughly act as turbulent diffusion. Although (10) is often adopted in second-order closure modeling, Moeng and Wyngaard (1989) and Mironov (2009) find the downgradient model is generally inadequate for detailed modeling of vertical transport in a highly convective atmospheric boundary layer. The LES finds turbulent transport T is a critical process in oceanic frontogenesis, and as a result, modeling of T is a challenge for parameterization schemes with varying stratification. Mean advection of turbulence A is small but also acts similar to T near the water surface.

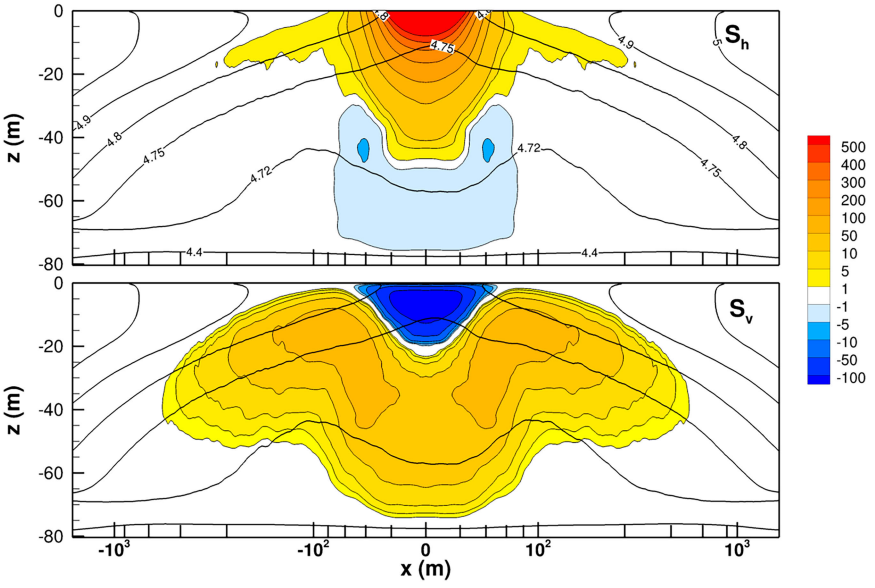

FIG. 15. (top) Horizontal and (bottom) vertical shear production (S_h, S_v) at t_p from case S100. The terms S_h and S_v are defined in (9). The panels are overlaid with identical line contours of the mean thermal structure $\langle\theta(x, z) - \theta_{\text{ref}}\rangle$ (°C). Small values between ±1 are colored white.

e. Boundary layer restratification

The SC and turbulence can compete in the restratification of the boundary layer (e.g., Skyllingstad and Samelson 2020). Restratification is present in our simulations. For example, based on the TKE profiles the boundary layer depth $h = (-65, -25)$ m at $x = (-6, -2)$ km, respectively. At $x = -1$ km, the incoming boundary layer is split vertically; the turbulent layers in the regions $-20 < z < 0$ m and $-75 < z -40$ m are separated by a relatively weak turbulence zone $-40 < z < -20$ m. The shallowing of the boundary layer and, in particular, the spatial extent of restratification is somewhat surprising. Vertical profiles of mean temperature

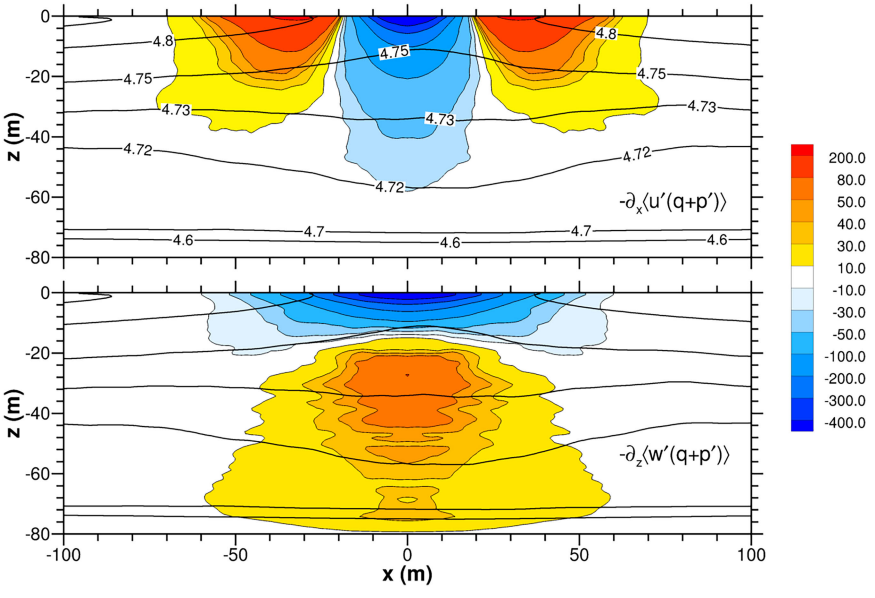

FIG. 16. Turbulent and pressure transport terms near the front centerline at t_p. Shown are (top) $-\partial_x\langle u'(q + p')\rangle$ and (bottom) $-\partial_z\langle w'(q + p')\rangle$. TKE $q = u_i'u_i'/2$ and terms are normalized by $w_*^3/|h_i|$ from case S100. The panels are overlaid with identical line contours of the mean thermal structure $\langle\theta(x, z) - \theta_{\text{ref}}\rangle$ (°C).

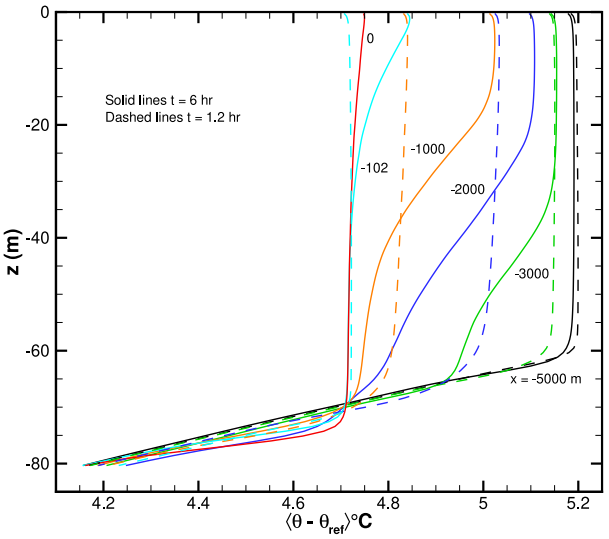

FIG. 17. Vertical profiles of mean temperature $\langle\theta - \theta_{\rm ref}\rangle$ at locations $x = -(5000, 3000, 2000, 1000, 102, 0)$ m left of the front centerline; line colors are black, green, blue, orange, cyan, red, respectively. Dashed and solid lines are $t = (1.2, 6)$ h, respectively. Notice the warming of the upper layer and cooling of the lower layer as time increases, creating a stably stratified interior.

$\langle\theta(x, z)\rangle$ in Fig. 17 illustrate the impact of the restratification process on the thermal structure in the boundary layer outside of the frontal zone. Restratification impacts turbulence dynamics: the vertical temperature flux $\langle w'\theta'\rangle$ and the vertical velocity variance highlight a transition to stable stratification and turbulence quenching in the boundary layer interior left and right of the front centerline (Fig. 18). Based on the x–z contours of $\langle w'^2\rangle$, the boundary layer depth in the farfield $x \simeq -6$ km is -65 m or more. Slightly outside the filament centerline $x \simeq -500$ m, the boundary layer shallows to approximately -10 m. Horizontal divergence of mean temperature flux $-\langle u\rangle\partial_z\langle\theta\rangle$ warms the top layer and cools the bottom layer, effectively shutting off convection in the boundary layer interior (Fig. 19). Thus, the SC impact on the OBL turbulence extends well beyond the frontal zone. However, because of strong downwelling in frontogenesis the boundary layer directly beneath the front is deeper than in the farfield. The restratification process depends on filament strength M^2/f^2 as shown in the lower panels of Figs. 19 and 18; the horizontal transport of cold water is weaker with decreasing filament strength and thus the region of stable stratification in the OBL is nearer the front.

A restratification ratio scaling for the rate of convective mixing versus filament secondary circulation usefully delineates the balance of these processes in these simulations. Skyllingstad and Samelson (2020), using results from Fox-Kemper et al. (2008) and Mahadevan et al. (2010), define the restratification ratio as

$$\mathscr{R} = \frac{f}{M^4|h|^2}\frac{Q_*\beta g}{\rho_o c_p}, \tag{11}$$

where $Q_*\beta g/\rho_o c_p$ is the surface flux expressed in buoyancy units and h is the mixed layer depth. The studies mentioned above are for baroclinically unstable fronts, but the competition between turbulent mixing and $\langle w'b'\rangle$ still exists in our regime. Mahadevan et al. (2010) and Skyllingstad and Samelson (2020) report that $\mathscr{R} < 0.06$ generates active restratification while $\mathscr{R} > 0.06$ suppresses restratification. For cases (S100, W100) with $h = 60$ m, $\mathscr{R} = (0.0014, 0.0111)$, respectively, and hence turbulence will not prevent restratification in Fig. 18. Note $\mathscr{R}$ is nearly 10 times larger in case W100 compared to case S100 given the same level of surface cooling, and the restratification is weaker and confined nearer the frontal zone compared to case S100. On the other hand, for case VW100 $\mathscr{R} = 0.229$, thus restratification is predicted to be suppressed; recall in Fig. 3 frontogenesis is not found over the integration time period of 104 h. With weak initial fluctuations, even longer integration periods are needed for a submesoscale filament to undergo symmetric and then baroclinic instability (e.g., Hamlington et al. 2014; Skyllingstad and Samelson 2020). Note the estimate (11) is qualitative because it is derived from simulations with no background turbulence at the onset, which differs from the present set of simulations.

f. *Cross-scale energy transfer*

An important topic is the scale content of the variances, fluxes, and in particular how energy is transferred among submesoscale and boundary layer spatial scales at the time of peak frontal strength. We assume that a horizontal scale $\delta = 50$ m provides an approximate separation between submesoscale and boundary layer motions, i.e., large and small scales, respectively, see Fig. 5. The LES fields from case S100 are filtered in x–y planes using a 2D Gaussian filter with scale δ; this filtering is smooth in wavenumber and physical space (e.g., Pope 2000, p. 563). The notation $\hat{()}$ denotes the spatial filtering, for example, vertical velocity $w = \hat{w} + w''$ where $(\hat{w}, w'')$ denote the (large, small) scale vertical motions, respectively. The filter width $\delta = 50$ m is larger than the LES mesh scale Δ, i.e., $\delta \gg \Delta$. As a result, the magnitude of the SGS fluxes τ_{ij} at scale Δ are considerably smaller compared to resolved Leonard fluxes,

$$T_{ij} = \widehat{u_i u_j} - \hat{u}_i\hat{u}_j. \tag{12}$$

Decomposition of the vertical velocity into large and small scales near the water surface from case S100 is shown in Fig. 20. Inspection of the results shows the motions are spatially correlated, and generally rotated clockwise. However, the small-scale vertical motions are more than a factor of 3 larger in magnitude. Notice the downwelling and upwelling spots in the vertical velocity field cross over the filament centerline $x = 0$. Turbulent large-scale horizontal motions left and right of the filament axis generate transient stagnation zones along the filament axis resulting in divergence and convergence, this leads to the downwelling and upwelling in the vertical velocity field observed in Fig. 20. Also, the divergence and convergence of the fluctuating horizontal motions generate significant horizontal momentum flux and variance ($u'v' < 0$ and $u'u' > 0$) along the filament axis

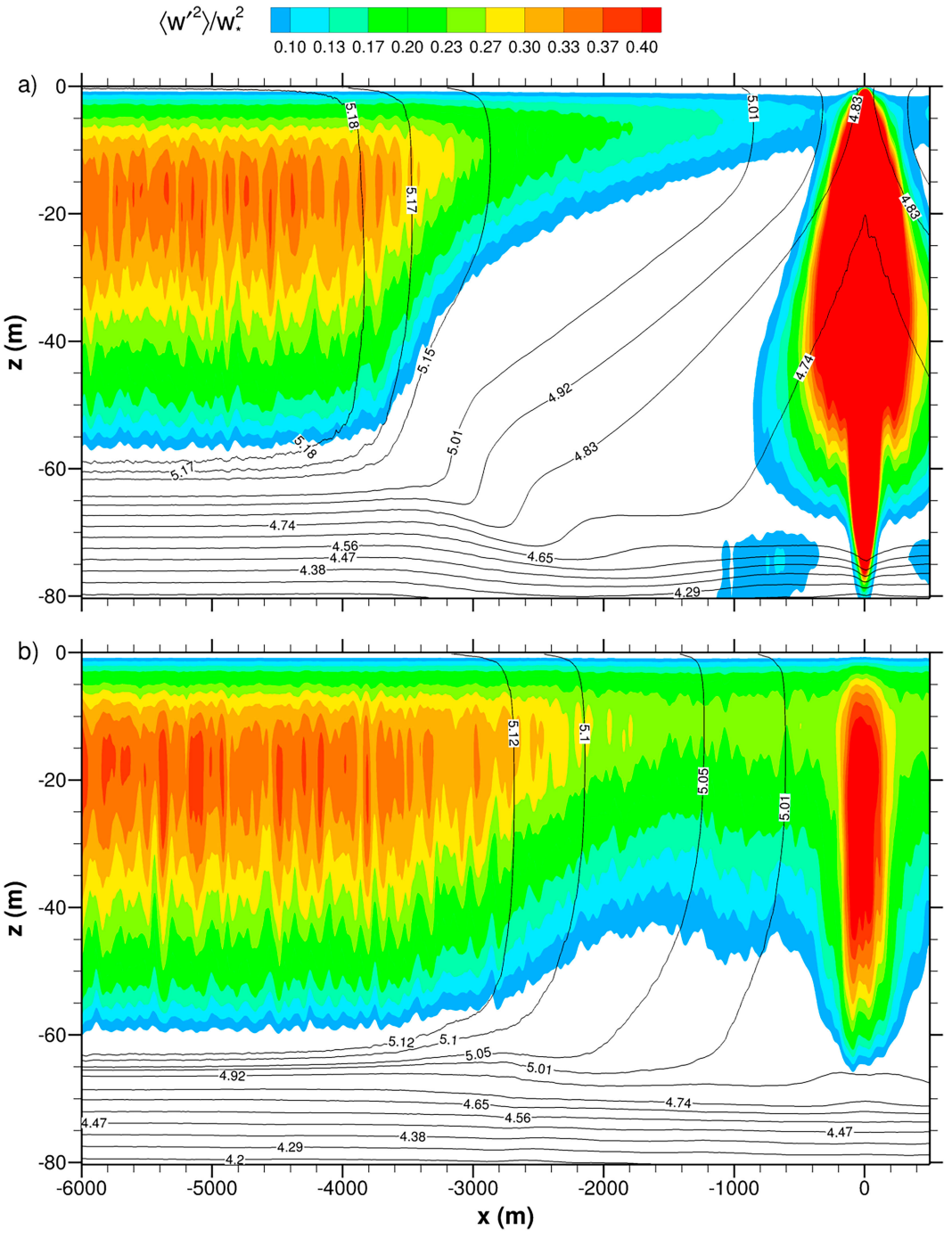

FIG. 18. Variation of resolved vertical variance $\langle w'^2\rangle/w_*^2$ in an x–z plane left of the front centerline. The colors are saturated for large values to emphasize the changes away from the front. Results from cases (a) S100 and (b) W100 are shown at their respective t_p values. Notice the shallowing of the boundary layer depth as the frontal zone is approached, especially for case S100 (a). Inside the front $x = [-200, 200]$ m the boundary layer deepens under the action of frontogenesis. The average thermal structure $\langle\theta - \theta_{\text{ref}}\rangle$ (°C) is shown by the overlaying line contours.

(Figs. 7 and 8). The magnitude ordering of the fluxes is $\langle u'v'\rangle \gg \langle v'w'\rangle > \langle u'w'\rangle$. Thus, large scales are the dominant contributors to the horizontal flux while the coupling between submesoscale motions and small-scale vertical turbulence at δ generates vertical fluxes, also see Fig. 20. Thus, a lateral shear instability generates large-scale motions that couple and cascade down to small-scale turbulence as depicted in Fig. 1.

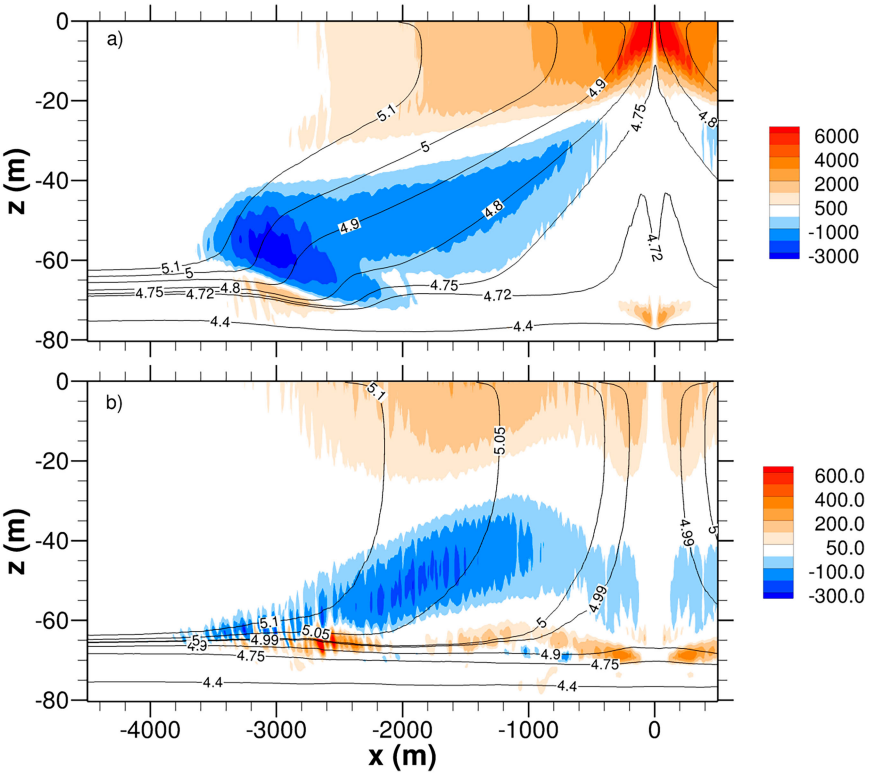

FIG. 19. Mean horizontal advection of temperature $-\langle u\rangle\partial_x\langle\theta\rangle$ normalized by $Q_*/|h_i|$ at t_p. The temperature time tendency $\partial_t\langle\theta\rangle > 0$ in the layer top, and $\partial_t\langle\theta\rangle < 0$ in the layer bottom because of horizontal advection of warm and cool water, respectively. (a) Case S100 and (b) case W100. The panels are overlaid with line contours of the mean thermal structure $\langle\theta - \theta_{\text{ref}}\rangle$ (°C).

To quantify the energy transfer we next examine the energy equation for the large scales. The energy equation for $\hat{u}_i$ (e.g., Tennekes and Lumley 1972, p. 62) is obtained by first filtering (2a) at scale δ followed by multiplication by $\hat{u}_i$, and SGS stresses τ_{ij} are neglected. These manipulations lead to

$$\frac{\partial\hat{k}}{\partial t} = \cdots + T_{ij}S_{ij}, \tag{13}$$

where the kinetic energy of the resolved motions $\hat{k} = \hat{u}_i\hat{u}_i/2$. The filtered strain rate S_{ij} is

$$S_{ij} = \frac{1}{2}\left(\frac{\partial\hat{u}_i}{\partial x_j} + \frac{\partial\hat{u}_j}{\partial x_i}\right). \tag{14}$$

The term $T_{ij}S_{ij}$ is the key energy transfer mechanism between large and small scales across δ (e.g., Wyngaard 2002). In physical space, $T_{ij}S_{ij}$ can be positive or negative instantaneously [i.e., transferring energy down (forward scatter) or up (backscatter) "cascades" across scales; e.g., Piomelli et al. 1991, 1996].

The average forward scatter and backscatter of the energy transfer $T_{ij}S_{ij}$ is depicted in Fig. 21. The energy transfer is further decomposed into vertical and horizontal components in Fig. 22. As expected in the inertial range at scale $\delta = 50$ m, forward scatter dominates the energy cascade. However, persistent energy backscatter from the boundary layer turbulence to larger submesoscale motions is found at the downwelling site along the filament centerline. Further interrogation shows the relatively small backscatter is concentrated in the vertical components of the energy transfer and in particular $T_{33}S_{33}$. The backscatter appears to be a consequence of the large vertical velocity variance in filament frontogenesis. Recall from Fig. 7, the turbulence variance $\langle w'^2\rangle$ is nearly a factor of 10 larger than its SC counterpart $\langle w\rangle^2$.

g. *Turbulence viscosities*

By long practice eddy viscosities (i.e., minus the ratio of turbulent flux to mean gradient) provide a language for summarizing the transport and energy conversion characteristics of the turbulence. It also has often been found to be a useful parameterization framework in non-LES models that do not resolve the turbulence but require its effects to be represented (e.g., Large et al. 1994). We end this section with two viscosity diagnoses. One is the momentum-flux viscosity related to the energy-production interaction of the total turbulence with the along-filament-averaged flow Figs. 12 and 13–15, and the other is related to the turbulent TKE transport Fig. 16.

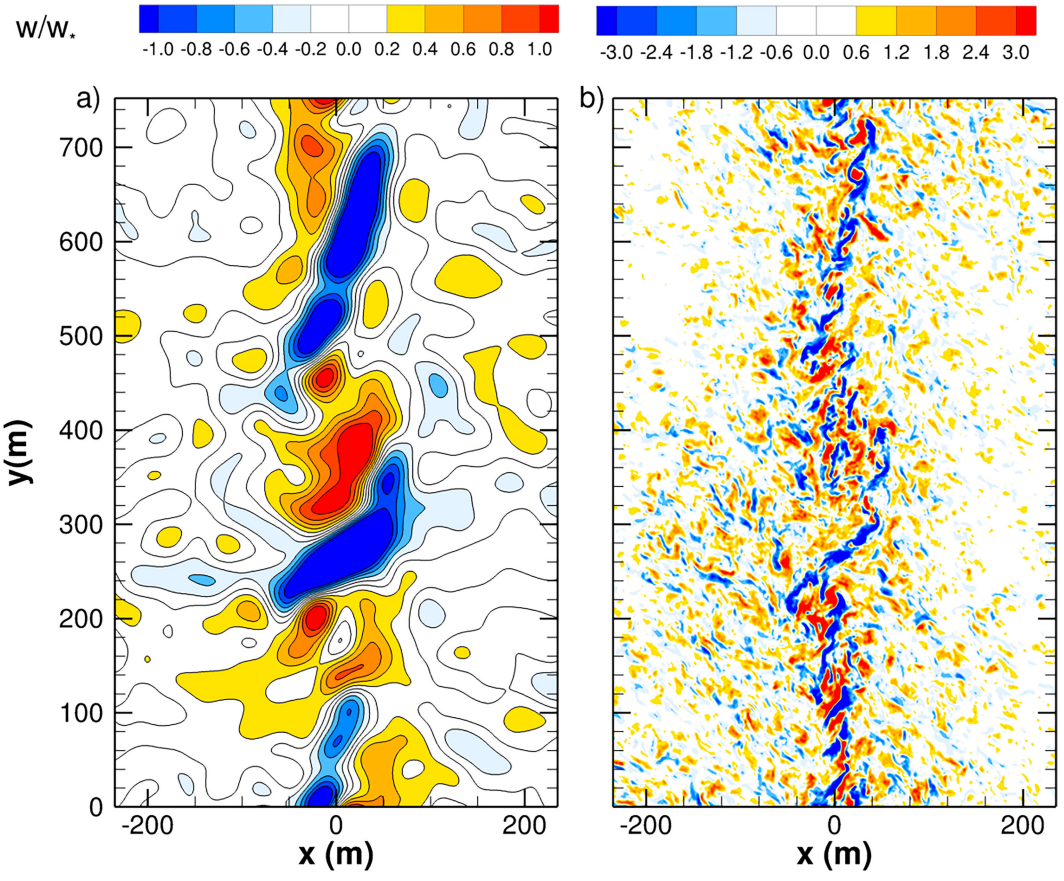

FIG. 20. Decomposition of the vertical velocity w into (a) large and (b) small scales near the water surface $z = -10.5$ m along the filament centerline at t_p. The filter width $\delta = 50$ m, the x–y aspect ratio of the panels is unity, and the range of the color bar changes between the panels.

For the TKE energy production, we define separate bulk viscosities for the horizontal and vertical momentum fluxes. The vertical and horizontal viscosities (K_v, K_h) are estimated from the TKE shear production terms (9) and the magnitude of their respective horizontal and vertical shear gradients:

$$\langle u'u'\rangle\frac{\partial\langle u\rangle}{\partial x} + \langle u'v'\rangle\frac{\partial\langle v\rangle}{\partial x} = -K_h\left[\left(\frac{\partial\langle u\rangle}{\partial x}\right)^2 + \left(\frac{\partial\langle v\rangle}{\partial x}\right)^2\right] \quad (15a)$$

$$\langle u'w'\rangle\frac{\partial\langle u\rangle}{\partial z} + \langle v'w'\rangle\frac{\partial\langle v\rangle}{\partial z} = -K_v\left[\left(\frac{\partial\langle u\rangle}{\partial z}\right)^2 + \left(\frac{\partial\langle v\rangle}{\partial z}\right)^2\right]. \quad (15b)$$

This formulation yields scalar viscosities by combining the two horizontal coordinate directions, and it partly mirrors the energy production terms in the numerators, S_h and S_v in Fig. 15. The x–z spatial variations of K_v and K_h are displayed in Fig. 23, nondimensionalized by the mixing-length scale for convection, $w_*|h_i| \approx 0.82\,\mathrm{m^2\,s^{-1}}$. Inspection of the results shows that the extrema are quite large, more than 100, within the frontal zone. Also, $K_h > K_v$, which is anticipated given the large magnitude of the horizontal frontal gradients $\partial_x\langle u, v\rangle$ and flux and variance $\langle u'v', u'u'\rangle$; recall that the horizontal flux and variance in Figs. 7 and 8 are also large compared to the vertical fluxes $\langle u'w', v'w'\rangle$. In the bulk of the OBL positive K_v implies a downgradient relationship between the vertical fluxes and vertical shear as in a horizontally homogeneous boundary layer. The K_v peaks in the middle of the boundary layer (as in the K-profile parameterization), and it decays smoothly with increasing distance from the filament axis. The K_h also is largest in the frontal zone, but its spatial structure is less simple. In the upper OBL the sign of the horizontal fluxes and horizontal shear are strongly downgradient with positive K_h. However, $K_h < 0$ is countergradient in the lower boundary layer. The horizontal variance is weakly positive $\langle u'^2\rangle \approx$ [2–5] (Fig. 7) where the lower branch of the SC (Fig. 2) is diverging away from the filament centerline, thus $K_h \approx -\langle u'^2\rangle/\partial_x\langle u\rangle < 0$. The horizontal flux $\langle u'v'\rangle \approx 0$ for $z < -40$ m (Fig. 8) and thus does not contribute to K_h.

Eddy viscosities (μ_v, μ_h) for the triple moments in (10) are next shown in Fig. 24. These viscosities are computed from (10) with the gradients $\partial_x\langle q\rangle$ and $\partial_z\langle q\rangle$ first smoothed in the x direction using a running average with width 50 m. The viscosities are positive and similarly large in magnitude, both to each other and to the momentum viscosities. The μ_h is

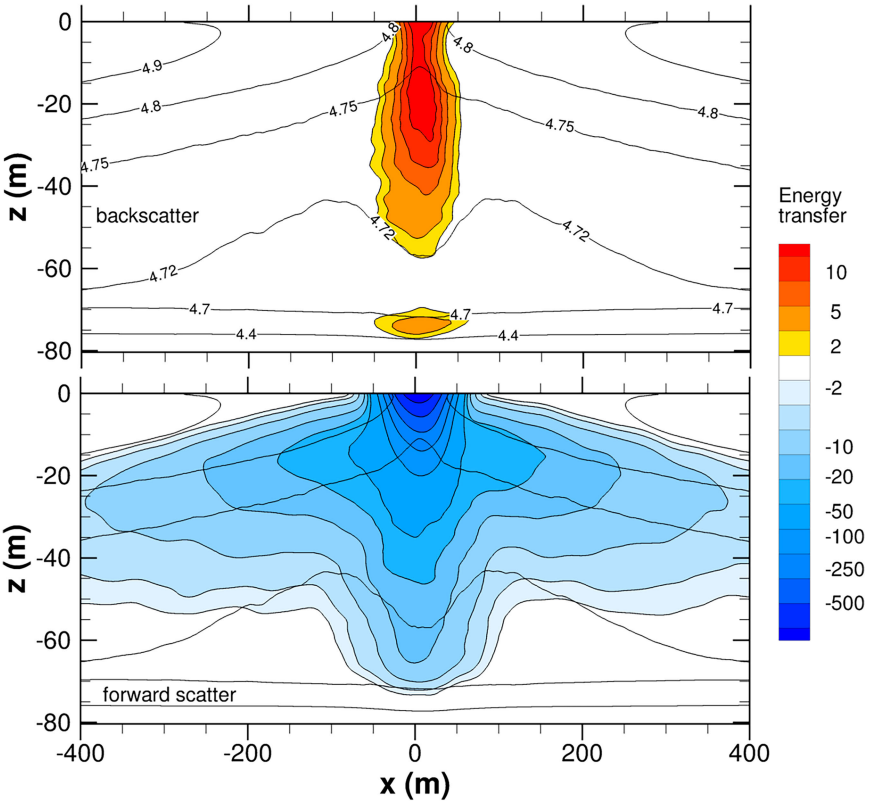

FIG. 21. Total energy transfer $\langle T_{ij}S_{ij}\rangle$ from large to small scales at scale $\delta = 50$ m in case S100 at t_p. The transfer is decomposed into (top) backscatter (positive values) and (bottom) forward scatter (negative values). The sum of the forward scatter and backscatter is negative. The panels are overlaid with identical line contours of the mean thermal structure $\langle \theta - \theta_{\text{ref}}\rangle$ (°C).

strongly concentrated near the upper surface, while μ_v peaks at middepth, i.e., the reversal of the (K_h, K_v) vertical structures. Their positivity confirms our interpretation that T in Figs. 13 and 14 act mainly as a diffusion process in the frontal zone. Note (μ_v, μ_h) are entirely positive in the frontal zone in contrast to the momentum viscosity K_h.

In summary, both the turbulent momentum flux and energy transport viscosities are mostly consistent with downgradient flux but are highly elevated in magnitude within the frontal zone, as is the TKE itself, and have nontrivial spatial structure. Useful parameterization formulas are not readily apparent.

6. Summary and conclusions

Turbulence in a submesoscale dense (cold) filament undergoing cold filament frontogenesis (CFF) in the upper-ocean boundary layer (OBL) is examined using results from a database of fine-mesh turbulence-resolving three-dimensional large-eddy simulations (LES; SM18; SM19). The analysis focuses on simulations with variable surface cooling Q_* (no surface winds) and initial filament strength M^2. The life cycle for these cases is initiation (density gradient plus background strain flow or TTW momentum mixing) → frontogenesis through secondary circulation (especially surface convergence) → frontal instability (mostly horizontal shear instability so far) → frontal arrest by opposing horizontal eddy momentum and buoyancy fluxes → slow frontal decay, plus possible bailouts at any stage into a thermal wind stationary front if the strain or turbulence go away. Surface convergence in the secondary circulation, $\delta = \nabla^h \cdot \mathbf{u}^h < 0$ where $\mathbf{u}^h$ are horizontal currents is the primary accelerant; CFF pathways are depicted in Fig. 1. We presume that a filament and one-side front evolve in qualitatively similar ways, although this has not yet been tested by us.

The process CFF is robust across a wide range of initial filament strength M^2 and surface cooling Q_* values, with essentially similar patterns to the fields but variable magnitudes and rates. The M^2 dependency is strong: bigger initial M^2 causes faster frontogenesis and earlier arrest with higher values of peak vertical vorticity ζ_{peak} and turbulence kinetic energy TKE_{peak}. The Q_* dependency is much weaker in these bulk measures but evident in some aspects of the shapes of the fields, e.g., at peak frontal strength. Very weak filaments with surface cooling (e.g., case VW100) do not exhibit CFF over a time period of more than 104 h. Although turbulent diffusion gradually weakens the underlying geostrophic jets and cold filament, their signatures obtained by space averaging

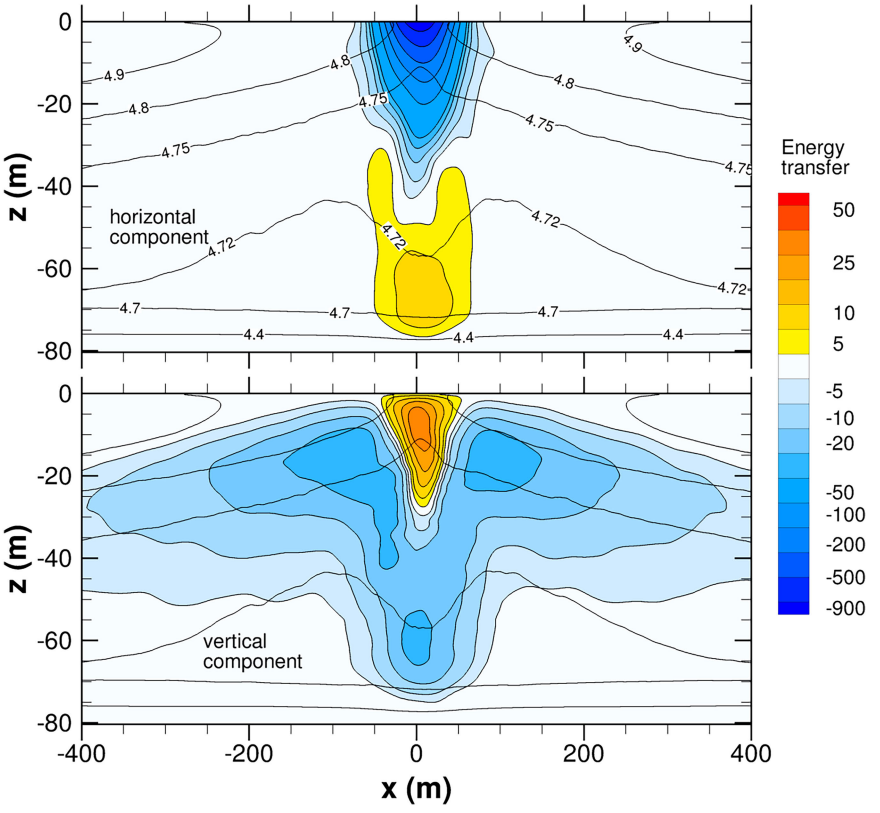

FIG. 22. Decomposition of the total energy transfer into vertical and horizontal components at a scale $\delta = 50$ m in case S100 at t_p. (top) Transfer from horizontal components $\langle T_{11}S_{11} + 2T_{12}S_{12} + T_{33}S_{33}\rangle$ and (bottom) transfer from vertical components $\langle 2T_{13}S_{13} + 2T_{23}S_{23} + T_{33}S_{33}\rangle$. Notice the average backscatter in the vertical component near the water surface, which is mainly due to $\langle T_{33}S_{33}\rangle$. The panels are overlaid with identical line contours of the mean thermal structure $\langle \theta - \theta_{\text{ref}}\rangle$ (°C).

remain identifiable for a long time. The $Q_* \to 0$ limit is consistent with the possibility of a stationary front in thermal wind balance.

Background boundary layer turbulence is woven into the CFF life cycle. In the present LES, convectively driven turbulence kick-starts frontogenesis by creating vertical momentum fluxes $\langle u'w', v'w'\rangle$ that couple the horizontal currents $\langle u, v\rangle$ resulting in net secondary circulations $\langle u, w\rangle$ in an x–z plane. The secondary circulation (SC) in the surface boundary layer is frontogenetic, and it remains coherent against a background of fully developed turbulence generated by surface cooling. Frontal instability occurs at the submesoscale with an alongfront scale much larger than the boundary layer depth. In all our cases so far, there is a horizontal shear instability of the sharpening front, especially $\partial_x\langle v\rangle$. Horizontal shear instability of the alongfront flow $\langle v(x, z)\rangle$ is common and can lead to arrest by horizontal turbulence flux $\langle u'v'\rangle$. That turbulence overtakes frontogenesis to cause arrest indicates that the turbulence growth rate is even faster than the frontogenetic rate.

During the arrest and decay stage, there is a forward energy cascade with an approximate $k_y^{-5/3}$ Kolmogorov-like shape at smaller scales. The frontal turbulence (FT) spectrum is broad with forward cascade from submesoscale down to dissipation. Energy transfer at a horizontal scale of ~50 m transitioning across the submesoscale–turbulence boundary highlights the forward energy transfer. However, persistent backscatter of energy (up the cascade) occurs along the filament centerline associated with gradients and fluxes in the vertical velocity, i.e., in the vertical component of the energy transfer $T_{33}S_{33}$.

The SC variances and fluxes of momentum and temperature are modestly larger than their turbulence counterparts. The notable exception is vertical velocity where the maximum turbulent variance is larger than the SC variance, $\langle w'^2\rangle \approx 10\langle w\rangle\langle w\rangle$. With large M^2, the turbulent variances and fluxes are tightly compacted to the frontal zone $-100 < x < 100$ m while the SC variances and fluxes are spread horizontally $-2000 < x < 2000$ km.

In the farfield, surface cooling drives turbulence, and the TKE balance is the familiar one with buoyant production B balancing dissipation D with turbulent and pressure transport T rearranging TKE in the vertical direction (e.g., Moeng and Wyngaard 1988). Near the filament centerline frontogenesis

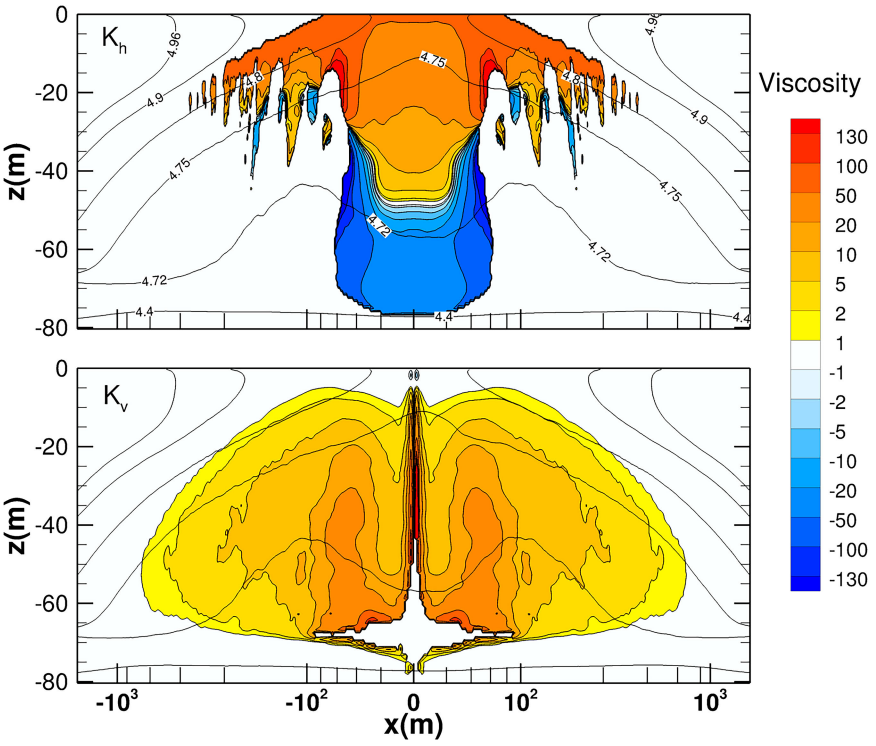

FIG. 23. Eddy viscosities (K_h, K_v) for the mean flow from case S100 at t_p. (top) Viscosity K_h is computed from the horizontal fluxes and horizontal shear, and (bottom) the vertical eddy viscosity K_v is computed from vertical fluxes and vertical shear; see (15). The viscosity is made dimensionless by $w_*|h_i| \approx 0.82\,\mathrm{m^2\,s^{-1}}$. The panels are overlaid with identical line contours of the mean thermal structure $\langle \theta - \theta_{\mathrm{ref}} \rangle$ (°C).

markedly changes the TKE balance with nonlocal transport T spreading away from the filament centerline. T and, to a much lesser extent, dissipation D balance shear production S. Shear production, which generates high levels of turbulence compared to the farfield, is mainly a consequence of horizontal gradients $\partial_x\langle u, v\rangle$ compared to vertical gradients $\partial_z\langle u, v\rangle$. Buoyancy and advection play a minor role in the TKE balance within the filament. The surprising TKE balance at the filament centerline remains with decreasing M^2. Even in a steady environment, there is great variety in frontal strength, frontogenetic rate, and arrest time. At arrest, both FT and SC have comparable KE within fronts. OBL restratification also occurs with varying distance depending on M^2. For example, high levels of M^2 with a potent SC can generate a shallow stable boundary layer outside the frontal zone with depth approximately 15% of its farfield value.

Horizontal heterogeneity in the initial buoyancy (temperature) field makes the turbulent OBL differ from its horizontally homogeneous counterpart. CFF generates horizontal and vertical eddy viscosities for momentum with $K_h \approx 10K_v$. Also, K_h is countergradient along the filament centerline below a depth $z < -40$ m, i.e., horizontal fluxes and mean gradients are of the same sign. Thus, the parameterization must be 3D (i.e., not just 1D vertical mixing) and have the primary effect of causing arrest in buoyancy $\langle b\rangle$ and $\langle v$ and dissipation of the submesoscale frontal flow if submesoscale frontal processes are resolved in the model. The horizontal and vertical components of the turbulent and pressure transport, $-\partial_x\langle u'(q' + p')\rangle$ and $-\partial_z\langle w'(q' + p')\rangle$ (i.e., the triple moments), are approximately represented as a downgradient diffusion process.

Thus, our view is that oceanic frontogenesis tends to have a generic life cycle in which the submesoscale front and boundary layer turbulence are closely interacting. As yet the frontogenetic stage is better understood than are the arrest, cascade, and decay processes, although all of these stages seem qualitatively plausible from a general perspective of fluid dynamical instabilities and turbulence.

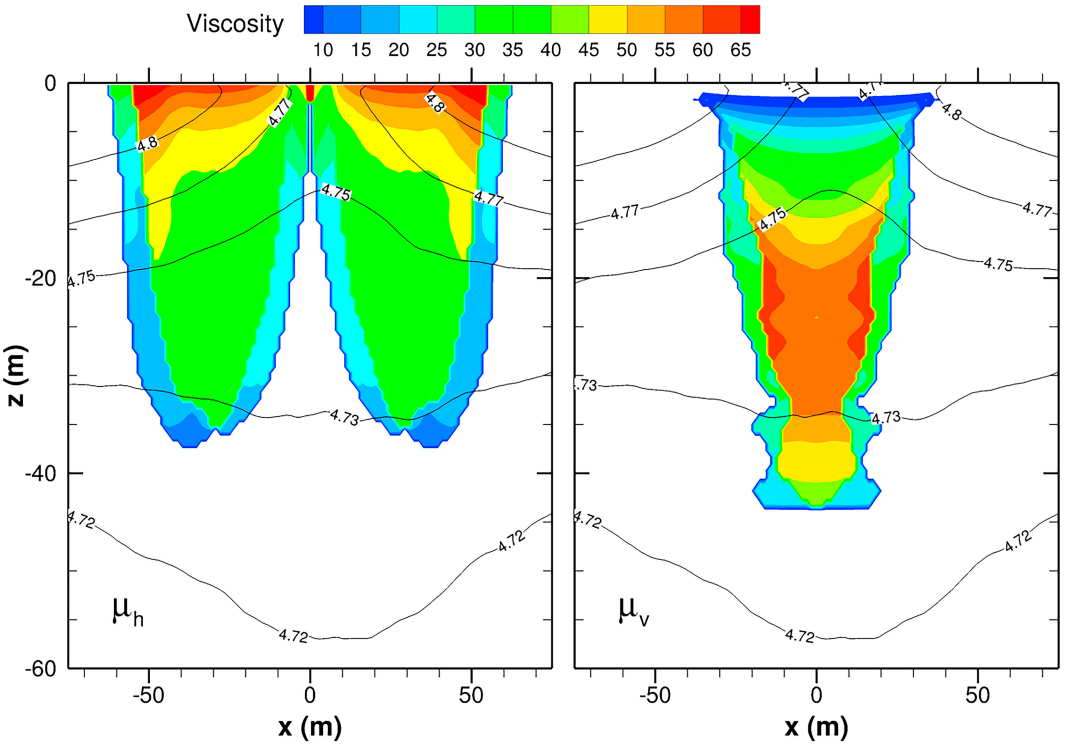

FIG. 24. Eddy viscosities (μ_h, μ_v) for turbulent transport terms, i.e., the triple moments in (7) and (10) from case S100 at t_p. The viscosity is made dimensionless by $w_*|h_i|$. The panels are overlaid with identical line contours of the mean thermal structure $\langle\theta - \theta_{\text{ref}}\rangle$ (°C).

Acknowledgments. P. P. S. and J. C. M. were supported by the Office of Naval Research through the Physical Oceanography Program Award N00014-17-1-2334 and N00014-18-1-2599, and by the National Oceanic and Atmospheric Administration Award NA19OAR4310378. P. P. S. acknowledges support from the National Science Foundation and the Geophysical Turbulence Program at the National Center for Atmospheric Research (NCAR). This research benefited greatly from computer resources provided by the Department of Defense High Performance Computing Modernization Program and NCAR's Computational and Information Systems Laboratory (https://doi.org/10.5065/D6RX99HX) sponsored by the National Science Foundation. We thank Baylor Fox-Kemper and another reviewer who provided comments that improved the manuscript.

Data availability statement. Simulation data are available on request.

REFERENCES

Aravind, H. M., V. Verma, S. Sarkar, M. A. Freilich, A. Mahadevan, P. J. Haley, P. F. J. Lermusiaux, and M. R. Allshouse, 2023: Lagrangian surface signatures reveal upper-ocean vertical displacement conduits near oceanic density fronts. *Ocean Modell.*, **181**, 102136, https://doi.org/10.1016/j.ocemod.2022.102136.

Bodner, A. S., B. Fox-Kemper, L. P. Van Roekel, J. C. McWilliams, and P. P. Sullivan, 2020: A perturbation approach to understanding the effects of turbulence on frontogenesis. *J. Fluid Mech.*, **883**, A25, https://doi.org/10.1017/jfm.2019.804.

——, ——, L. Johnson, L. P. V. Roekel, J. C. McWilliams, P. P. Sullivan, P. S. Hall, and J. Dong, 2023: Modifying the mixed layer eddy parameterization to include frontogenesis arrest by boundary layer turbulence. *J. Phys. Oceanogr.*, **53**, 323–339, https://doi.org/10.1175/JPO-D-21-0297.1.

Brucker, K. A., and S. Sarkar, 2007: Evolution of an initially turbulent stratified shear layer. *Phys. Fluids*, **19**, 105105, https://doi.org/10.1063/1.2756581.

Capó, E., and J. C. McWilliams, 2022: Coherent Lagrangian pathways near an East Alboran Front. *J. Geophys. Res. Oceans*, **127**, e2021JC018022, https://doi.org/10.1029/2021JC018022.

Cohen, J. H., A. M. Internicola, R. A. Mason, and T. Kukulka, 2019: Observations and simulations of microplastic debris in a tide, wind, and freshwater-driven estuarine environment: The Delaware Bay. *Environ. Sci. Technol.*, **53**, 14 204–14 211, https://doi.org/10.1021/acs.est.9b04814.

Crowe, M. N., and J. R. Taylor, 2018: The evolution of a front in turbulent thermal wind balance. Part 1. Theory. *J. Fluid Mech.*, **850**, 179–211, https://doi.org/10.1017/jfm.2018.448.

——, and ——, 2019: The evolution of a front in turbulent thermal wind balance. Part 2. Numerical simulations. *J. Fluid Mech.*, **880**, 326–352, https://doi.org/10.1017/jfm.2019.688.

Csanady, G. T., 1973: *Turbulent Diffusion in the Environment*. D. Reidel Publishing Company, 248 pp.

D'Asaro, E., C. Lee, L. Rainville, R. Harcourt, and L. Thomas, 2011: Enhanced turbulence and energy dissipation at ocean fronts. *Science*, **332**, 318–322, https://doi.org/10.1126/science.1201515.

——, and Coauthors, 2018: Ocean convergence and the dispersion of flotsam. *Proc. Natl. Acad. Sci. USA*, **115**, 1162–1167, https://doi.org/10.1073/pnas.1718453115.

Dingwall, J., T. Chor, and J. R. Taylor, 2023: Large eddy simulations of the accumulation of buoyant material in oceanic wind-driven and convective turbulence. *J. Fluid Mech.*, **954**, A27, https://doi.org/10.1017/jfm.2022.969.

Fox-Kemper, B., R. Ferrari, and R. Hallberg, 2008: Parameterization of mixed layer eddies. Part I. Theory and diagnosis. *J. Phys. Oceanogr.*, **38**, 1145–1165, https://doi.org/10.1175/2007JPO3792.1.

Freilich, M., and A. Mahadevan, 2022: Coherent pathways for subduction from the surface mixed layer at ocean fronts. *J. Geophys. Res. Oceans*, **126**, e2020JC017042, https://doi.org/10.1029/2020JC017042.

Gula, J., M. J. Molemaker, and J. C. McWilliams, 2014: Submesoscale cold filaments in the Gulf Stream. *J. Phys. Oceanogr.*, **44**, 2617–2643, https://doi.org/10.1175/JPO-D-14-0029.1.

——, J. Taylor, A. Shcherbina, and A. Mahadevan, 2021: Submesoscale processes and mixing. *Ocean Mixing: Drivers, Mechanisms and Impacts*, M. P. Meredith and A. N. Garabato, Eds., Elsevier, 181–214.

Hamlington, P. E., L. P. Van Roekel, B. Fox-Kemper, K. Julien, and G. P. Chini, 2014: Langmuir-Submesoscale interactions: Descriptive analysis of multiscale frontal spindown simulations. *J. Phys. Oceanogr.*, **44**, 2249–2272, https://doi.org/10.1175/JPO-D-13-0139.1.

Hoskins, B., 2003: Back to frontogenesis. *A Half Century of Progress in Meteorology: A Tribute to Richard Reed*, *Meteor. Monogr.*, No. 53, Amer. Meteor. Soc., 49–60.

——, and F. P. Bretherton, 1972: Atmospheric frontogenesis models: Mathematical formulation and solution. *J. Atmos. Sci.*, **29**, 11–37, https://doi.org/10.1175/1520-0469(1972)029<0011:AFMMFA>2.0.CO;2.

Hussain, A. K. M. F., and W. C. Reynolds, 1970: The mechanics of an organized wave in turbulent shear flow. *J. Fluid Mech.*, **41**, 241–258, https://doi.org/10.1017/S0022112070000605.

Johnston, T. M. S., D. L. Rudnick, G. S. Carter, R. E. Todd, and S. T. Cole, 2011: Internal tidal beams and mixing near Monterey Bay. *J. Geophys. Res.*, **116**, C03017, https://doi.org/10.1029/2010JC006592.

Kaminski, A. K., and W. D. Smyth, 2019: Stratified shear instability in a field of pre-existing turbulence. *J. Fluid Mech.*, **862**, 639–658, https://doi.org/10.1017/jfm.2018.973.

Kukulka, T., and K. Brunner, 2015: Passive buoyant tracers in the ocean surface boundary layer: 1. Influence of equilibrium wind-waves on vertical distributions. *J. Geophys. Res. Oceans*, **120**, 3837–3858, https://doi.org/10.1002/2014JC010487.

Large, W. G., J. C. McWilliams, and S. C. Doney, 1994: Oceanic vertical mixing: A review and a model with a nonlocal boundary layer parameterization. *Rev. Geophys.*, **32**, 363–403, https://doi.org/10.1029/94RG01872.

Mahadevan, A., A. Tandon, and R. Ferrari, 2010: Rapid changes in mixed layer stratification driven by submesoscale instabilities and winds. *J. Geophys. Res.*, **115**, C03017, https://doi.org/10.1029/2008JC005203.

McWilliams, J. C., 2016: Submesoscale currents in the ocean. *Proc. Roy. Soc. London*, **472A**, 20160117, http://dx.doi.org/10.1098/rspa.2016.0117.

——, 2017: Submesoscale surface fronts and filaments: Secondary circulation, buoyancy flux, and frontogenesis. *J. Fluid Mech.*, **823**, 391–432, https://doi.org/10.1017/jfm.2017.294.

——, 2018: Surface wave effects on submesoscale fronts and filaments. *J. Fluid Mech.*, **843**, 479–517, https://doi.org/10.1017/jfm.2018.158.

——, 2021: Oceanic frontogenesis. *Annu. Rev. Mar. Sci.*, **13**, 227–253, https://doi.org/10.1146/annurev-marine-032320-120725.

——, and B. Fox-Kemper, 2013: Oceanic wave-balanced surface fronts and filaments. *J. Fluid Mech.*, **730**, 464–490, https://doi.org/10.1017/jfm.2013.348.

——, P. P. Sullivan, and C.-H. Moeng, 1997: Langmuir turbulence in the ocean. *J. Fluid Mech.*, **334**, 1–30, https://doi.org/10.1017/S0022112096004375.

——, M. J. Molemaker, and E. I. Olafsdottir, 2009: Linear fluctuation growth during frontogenesis. *J. Phys. Oceanogr.*, **39**, 3111–3129, https://doi.org/10.1175/2009JPO4186.1.

——, J. Gula, M. J. Molemaker, L. Renault, and A. F. Shchepetkin, 2015: Filament frontogenesis by boundary layer turbulence. *J. Phys. Oceanogr.*, **45**, 1988–2005, https://doi.org/10.1175/JPO-D-14-0211.1.

Mironov, D. V., 2009: Turbulence in the lower troposphere: Second-order closure and mass-flux modelling frameworks. *Interdisciplinary Aspects of Turbulence*, W. Hillebrandt and F. Kupka, Eds., Lecture Notes in Physics, Vol. 756, Springer-Verlag, 161–221.

Moeng, C.-H., 1984: A large-eddy simulation model for the study of planetary boundary-layer turbulence. *J. Atmos. Sci.*, **41**, 2052–2062, https://doi.org/10.1175/1520-0469(1984)041<2052:ALESMF>2.0.CO;2.

——, and J. C. Wyngaard, 1988: Spectral analysis of large-eddy simulations of the convective boundary layer. *J. Atmos. Sci.*, **45**, 3573–3587, https://doi.org/10.1175/1520-0469(1988)045<3573:SAOLES>2.0.CO;2.

——, and ——, 1989: Evaluation of turbulent transport and dissipation closures in second-order modeling. *J. Atmos. Sci.*, **46**, 2311–2330, https://doi.org/10.1175/1520-0469(1989)046<2311:EOTTAD>2.0.CO;2.

——, and P. P. Sullivan, 2015: Large-eddy simulation. *Encyclopedia of Atmospheric Sciences*, 2nd ed. G. R. North, F. Zhang and J. Pyle, Eds., Academic Press, 232–240, https://doi.org/10.1016/B978-0-12-382225-3.00201-2.

Pham, H. T., and S. Sarkar, 2018: Ageostrophic secondary circulation at a submesoscale front and formation of gravity currents. *J. Phys. Oceanogr.*, **48**, 2507–2529, https://doi.org/10.1175/JPO-D-17-0271.1.

——, and ——, 2019: The role of turbulence in strong submesoscale fronts of the Bay of Bengal. *Deep-Sea Res. II*, **168**, 104644, https://doi.org/10.1016/j.dsr2.2019.104644.

——, ——, L. Johnson, B. Fox-Kemper, P. P. Sullivan, and Q. Li, 2023: Multi-scale variability of turbulent mixing during a monsoon intraseasonal oscillation in the Bay of Bengal: An LES study. *J. Geophys. Res. Oceans*, **128**, e2022JC018959, https://doi.org/10.1029/2022JC018959.

Piomelli, U., W. H. Cabot, P. Moin, and S. Lee, 1991: Subgrid-scale backscatter in turbulent and transitional flows. *Phys. Fluids*, **3A**, 1766–1771, https://doi.org/10.1063/1.857956.

——, Y. Yu, and R. J. Adrian, 1996: Subgrid-scale energy transfer and near-wall turbulence structure. *Phys. Fluids*, **8**, 215–224, https://doi.org/10.1063/1.868829.

Pope, S. B., 2000: *Turbulent Flows*. Cambridge University Press, 771 pp.

Qu, L., and Coauthors, 2022: Rapid vertical exchange at fronts in the Northern Gulf of Mexico. *Nat. Commun.*, **13**, 5624, https://doi.org/10.1038/s41467-022-33251-7.

Samelson, R. M., and E. D. Skyllingstad, 2016: Frontogenesis and turbulence: A numerical simulation. *J. Atmos. Sci.*, **73**, 5025–5040, https://doi.org/10.1175/JAS-D-16-0145.1.

Skyllingstad, E. D., and R. M. Samelson, 2012: Baroclinic frontal instabilities and turbulent mixing in the surface boundary layer. Part I: Unforced simulations. *J. Phys. Oceanogr.*, **42**, 1701–1716, https://doi.org/10.1175/JPO-D-10-05016.1.

——, and ——, 2020: Instability processes in simulated finite-width ocean fronts. *J. Phys. Oceanogr.*, **50**, 2781–2796, https://doi.org/10.1175/JPO-D-20-0030.1.

——, J. Duncombe, and R. M. Samelson, 2017: Baroclinic frontal instabilities and turbulent mixing in the surface boundary layer. Part II: Forced simulations. *J. Phys. Oceanogr.*, **47**, 2429–2454, https://doi.org/10.1175/JPO-D-16-0179.1.

Snyder, C., 1998: Approximate dynamical equations for fronts modified by the planetary boundary layer. *J. Atmos. Sci.*, **55**, 777–787, https://doi.org/10.1175/1520-0469(1998)055<0777:ADEFFM>2.0.CO;2.

Spall, M. A., 1997: Baroclinic jets in confluent flow. *J. Phys. Oceanogr.*, **27**, 1054–1071, https://doi.org/10.1175/1520-0485(1997)027<1054:BJICF>2.0.CO;2.

Stull, R. B., 1988: *An Introduction to Boundary Layer Meteorology*. Kluwer Academic Publishers, 666 pp.

Sullivan, P. P., and J. C. McWilliams, 2018: Frontogenesis and frontal arrest of a dense filament in the oceanic surface boundary layer. *J. Fluid Mech.*, **837**, 341–380, https://doi.org/10.1017/jfm.2017.833.

——, and ——, 2019: Langmuir turbulence and filament frontogenesis in the oceanic surface boundary layer. *J. Fluid Mech.*, **879**, 512–553, https://doi.org/10.1017/jfm.2019.655.

——, ——, and C.-H. Moeng, 2000: Simulation of turbulent flow over idealized water waves. *J. Fluid Mech.*, **404**, 47–85, https://doi.org/10.1017/S0022112099006965.

——, ——, and W. K. Melville, 2007: Surface gravity wave effects in the oceanic boundary layer: Large-eddy simulation with vortex force and stochastic breakers. *J. Fluid Mech.*, **593**, 405–452, https://doi.org/10.1017/S002211200700897X.

——, ——, and E. G. Patton, 2014: Large eddy simulation of marine boundary layers above a spectrum of moving waves. *J. Atmos. Sci.*, **71**, 4001–4027, https://doi.org/10.1175/JAS-D-14-0095.1.

Suzuki, N., B. Fox-Kemper, P. E. Hamlington, and L. P. V. Roekel, 2016: Surface waves affect frontogenesis. *J. Geophys. Res. Oceans*, **121**, 3597–3624, https://doi.org/10.1002/2015JC011563.

Taylor, G. I., 1953: Dispersion of soluble matter in solvent flowing slowly through a tube. *Proc. Roy. Soc. London*, **219A**, 186–203, https://doi.org/10.1098/rspa.1953.0139.

Taylor, J. R., 2018: Accumulation and subduction of buoyant material at submesoscale fronts. *J. Phys. Oceanogr.*, **48**, 1233–1241, https://doi.org/10.1175/JPO-D-17-0269.1.

——, and A. F. Thompson, 2023: Submesoscale dynamics in the upper ocean. *Annu. Rev. Fluid Mech.*, **55**, 103–127, https://doi.org/10.1146/annurev-fluid-031422-095147.

Tennekes, H., and J. L. Lumley, 1972: *A First Course in Turbulence*. The MIT Press, 300 pp.

Thomas, L. N., and C. Lee, 2005: Intensification of ocean fronts by down-front winds. *J. Phys. Oceanogr.*, **35**, 1086–1102, https://doi.org/10.1175/JPO2737.1.

Thorncroft, C. D., B. J. Hoskins, and M. E. McIntyre, 1993: Two paradigms of baroclinic-wave life-cycle behaviour. *Quart. J. Roy. Meteor. Soc.*, **119**, 17–55, https://doi.org/10.1002/qj.49711950903.

Verma, V., H. T. Pham, and S. Sarkar, 2019: The submesoscale, the finescale and their interaction at a mixed layer front. *Ocean Modell.*, **140**, 101400, https://doi.org/10.1016/j.ocemod.2019.05.004.

——, ——, and ——, 2022: Interaction between upper-ocean submesoscale currents and convective turbulence. *J. Phys. Oceanogr.*, **52**, 437–458, https://doi.org/10.1175/JPO-D-21-0148.1.

Wenegrat, J. O., L. N. Thomas, M. A. Sundermeyer, J. R. Taylor, E. A. D'Asaro, J. M. Klymak, R. K. Shearman, and C. M. Lee, 2020: Enhanced mixing across the gyre boundary at the Gulf Stream Front. *Proc. Natl. Acad. Sci. USA*, **117**, 17 607–17 614, https://doi.org/10.1073/pnas.2005558117.

Wyngaard, J. C., 2002: On the mean rate of energy transfer in turbulence. *Phys. Fluids*, **14**, 2426–2431, https://doi.org/10.1063/1.1481745.

Young, W. R., 1994: The subinertial mixed layer approximation. *J. Phys. Oceanogr.*, **24**, 1812–1826, https://doi.org/10.1175/1520-0485(1994)024<1812:TSMLA>2.0.CO;2.

——, P. B. Rhines, and C. J. R. Garrett, 1982: Shear-flow dispersion, internal waves and horizontal mixing in the ocean. *J. Phys. Oceanogr.*, **12**, 515–527, https://doi.org/10.1175/1520-0485(1982)012<0515:SFDIWA>2.0.CO;2.

Yuan, J., and J.-H. Liang, 2021: Wind-and wave-driven ocean surface boundary layer in a frontal zone: Roles of submesoscale eddies and Ekman–Stokes transport. *J. Phys. Oceanogr.*, **51**, 2655–2680, https://doi.org/10.1175/JPO-D-20-0270.1.